

Scale dependence of earthquake rupture prestress in models with enhanced weakening: Implications for event statistics and inferences of fault stress

Valère Lambert¹ Nadia Lapusta^{1,2} Daniel Faulkner³

¹Seismological Laboratory, California Institute of Technology, Pasadena, California, USA

²Department of Mechanical and Civil Engineering, California Institute of Technology, Pasadena, California, USA

³School of Environmental Sciences, University of Liverpool, Liverpool, UK

Key Points:

- Local shear prestress varies significantly within and among ruptures, being close to the quasi-static fault strength in nucleation regions.
- Efficient weakening allows rupture propagation over areas of lower prestress, leading to lower average prestress over larger rupture areas.
- Fault models with more efficient dynamic weakening produce fewer smaller events and result in systematically lower b-values.

Corresponding author: Valère Lambert, vlambert@caltech.edu

This article has been accepted for publication and undergone full peer review but has not been through the copyediting, typesetting, pagination and proofreading process, which may lead to differences between this version and the Version of Record. Please cite this article as doi: [10.1029/2021JB021886](https://doi.org/10.1029/2021JB021886).

This article is protected by copyright. All rights reserved.

Accepted Article

16 **Abstract**

17 Determining conditions for earthquake slip on faults is a key goal of fault mechanics highly
18 relevant to seismic hazard. Previous studies have demonstrated that enhanced dynamic
19 weakening (EDW) can lead to dynamic rupture of faults with much lower shear stress
20 than required for rupture nucleation. We study the stress conditions before earthquake
21 ruptures of different sizes that spontaneously evolve in numerical simulations of earth-
22 quake sequences on rate-and-state faults with EDW due to thermal pressurization of pore
23 fluids. We find that average shear stress right before dynamic rupture (aka shear pre-
24 stress) systematically varies with the rupture size. The smallest ruptures have prestress
25 comparable to the local shear stress required for nucleation. Larger ruptures weaken the
26 fault more, propagate over increasingly under-stressed areas due to dynamic stress con-
27 centration, and result in progressively lower average prestress over the entire rupture.
28 The effect is more significant in fault models with more efficient EDW. We find that, as
29 a result, fault models with more efficient weakening produce fewer small events and re-
30 sult in systematically lower b-values of the frequency-magnitude event distributions. The
31 findings 1) illustrate that large earthquakes can occur on faults that appear not to be
32 critically stressed compared to stresses required for slip nucleation; 2) highlight the im-
33 portance of finite-fault modeling in relating the local friction behavior determined in the
34 lab to the field scale; and 3) suggest that paucity of small events or seismic quiescence
35 may be the observational indication of mature faults that operate under low shear stress
36 due to EDW.

37 **Plain Language Summary**

38 Understanding the evolution of stress on faults over periods of slow and fast mo-
39 tion is crucial for assessing how earthquakes start, grow, and ultimately stop. Here we
40 use computer models to explore the stress conditions required for simulated earthquake
41 ruptures to occur. We find that the critical stress conditions for rupture propagation de-
42 pend on the size of the rupture and how efficiently the fault shear resistance weakens dur-

43 ing fast slip. In particular, larger earthquakes on faults that experience increasingly more
44 efficient weakening during rupture can propagate under systematically lower stress con-
45 ditions than those required for rupture nucleation. As a result, we find that faults that
46 exhibit efficient weakening can host predominantly large earthquakes at the expense of
47 smaller earthquakes. Our findings illustrate how large earthquakes can occur on faults
48 that appear to be understressed compared to expected conditions for rupture nucleation.
49 Moreover, our findings support a body of work suggesting that the scarcity of small earth-
50 quakes on some major mature fault segments, like the central section of the San Andreas
51 Fault, may indicate that they experience substantial weakening during large earthquakes,
52 a consideration that may be particularly useful for earthquake early warning systems.

53 1 Introduction

54 Determining the absolute level and controlling factors of the stress state on faults
55 has profound implications for earthquake physics, seismic hazard assessment, and the
56 role of faulting in plate tectonics and geodynamics. Numerous lines of field evidence sug-
57 gest that the average shear stress acting on mature faults must be low, 20 MPa or less,
58 in comparison to the expected shear resistance of 100 - 200 MPa averaged over the seis-
59 mogenic depth, given rock overburden and hydrostatic pore fluid pressure, along with
60 typical quasi-static friction coefficients of 0.6 - 0.85 (aka "Byerlee friction") measured
61 in laboratory experiments (Brune et al., 1969; Henyey & Wasserburg, 1971; Sibson, 1975;
62 Byerlee, 1978; Lachenbruch & Sass, 1980; Townend & Zoback, 2004; Rice, 2006; Suppe,
63 2007; Tanikawa & Shimamoto, 2009; Nankali, 2011; Fulton et al., 2013; Gao & Wang,
64 2014). Such evidence includes the lack of a substantial heat flow anomaly around ma-
65 ture faults that would be expected for fault slip at 100 MPa or more (Brune et al., 1969;
66 Henyey & Wasserburg, 1971; Lachenbruch & Sass, 1980; Nankali, 2011; Gao & Wang,
67 2014), inferences of steep angles between the principal stress direction and fault plane
68 (Townend & Zoback, 2004), analyses of the fault core obtained by drilling through shal-
69 low parts of faults that have experienced major recent events, including the 2011 M_w

9.0 Tohoku-oki event (Tanikawa & Shimamoto, 2009; Fulton et al., 2013), the geometry of thrust-belt wedges (Suppe, 2007), and the existence of long-lived narrow shear zones that do not exhibit any evidence of melting (Sibson, 1975; Rice, 2006). Note that such evidence for apparent fault weakness pertains predominantly to mature faults, whereas some studies suggest that smaller, less mature faults may sustain the expected high shear stresses given Byerlee friction values and overburden minus hydrostatic pore pressure (e.g. Townend & Zoback, 2000).

A relatively straightforward explanation for the low-stress operation of mature faults is that they may be persistently weak (Figure 1), due to the presence of anomalously low quasi-static friction coefficients and/or low effective normal stress from pervasive fluid overpressure (Brown et al., 2003; Faulkner et al., 2006; Bangs et al., 2009; Collettini et al., 2009; Lockner et al., 2011). Mature fault zones typically have a layer of fine gouge material at their core (e.g., Faulkner et al., 2006). However, most materials with low quasi-static friction coefficients (less than 0.5) under laboratory conditions tend to exhibit velocity-strengthening behavior (Ikari et al., 2011), which would preclude spontaneous nucleation of dynamic ruptures. Moreover, while evidence of substantial fluid overpressure has been documented for many subduction zones (Brown et al., 2003; Bangs et al., 2009), there remains much debate over the ubiquity of chronic near-lithostatic fluid overpressurization along faults in other tectonic settings, such as continental faults, with some bore-hole measurements suggesting fluid pressure levels more consistent with hydrostatic conditions (Townend & Zoback, 2000; Zoback et al., 2010).

An alternative hypothesis for explaining such low-stress, low-heat operation is that mature faults are indeed strong at slow, quasi-static sliding rates but undergo considerable enhanced dynamic weakening at seismic slip rates, which has been widely hypothesized in theoretical studies and documented in laboratory experiments (Figure 1, dashed black line; Sibson, 1973; Tsutsumi & Shimamoto, 1997; Rice, 2006; Wibberley et al., 2008; Di Toro et al., 2011; Noda et al., 2009; Acosta et al., 2018). The presence of enhanced

dynamic weakening on natural faults can be questioned by the expectation that enhanced dynamic weakening would result in magnitude-dependent static stress drops (Beeler et al., 2012; Gao & Wang, 2014), with larger ruptures resulting in higher stress drops than typical values of 1 to 10 MPa inferred from earthquakes on natural faults (Allmann & Shearer, 2009; Ye et al., 2016b). The expectation is based on a common assumption that the shear prestress over the entire rupture area should be near the static strength of the fault while the final shear stress should be near the dynamic resistance of the fault, resulting in a large static stress change for more efficient weakening. However, a number of numerical and laboratory studies have demonstrated that, once nucleated, dynamic ruptures can propagate under regions with prestress conditions that are well below the expected static strength, based on prescribed or measured quasi-static friction coefficients and confining conditions (Zheng & Rice, 1998; Noda et al., 2009; Lu et al., 2010; Dunningham et al., 2011; Gabriel et al., 2012; Fineberg & Bouchbinder, 2015; Schmitt et al., 2015) while the final shear stress could be higher than dynamic shear stress for pulse-like ruptures, with both inferences promoting reasonable stress drops. Such studies have often considered a single dynamic rupture nucleated artificially and propagating over uniform prestress conditions.

Recent numerical studies of earthquake sequences have shown that fault models with a combination of both hypotheses for low-stress operation, including some chronic fluid overpressure as well as mild-to-moderate enhanced dynamic weakening due to the thermal pressurization of pore fluids, work well for reproducing a range of observations (Perry et al., 2020; Lambert et al., 2021). These include reasonable static stress drops between 1 - 10 MPa nearly independent of earthquake magnitude, the seismologically inferred increase in average breakdown energy with rupture size, the radiation ratios between 0.1 and 1 inferred for natural events, and the heat flow constraints. The simulations produce mainly crack-like or mild pulse-like ruptures, with no significant undershoot. The near magnitude-invariance of average static stress drop arises in these fault models because enhanced dynamic weakening results in both lower average prestress and

lower average final shear stress for larger ruptures with larger slip, with the average static stress drops being nearly magnitude-independent. These studies suggest that distinguishing between the conditions required for rupture nucleation and propagation is important for assessing the relationship between laboratory friction measurements, seismological observations and the absolute stress conditions on faults.

Here, we use and expand upon the set of numerical models from Perry et al. (2020) and Lambert et al. (2021) to document the variability of prestress on a fault that arises from the history of previous ruptures, and to study the relation between the size of dynamic rupture events and the average shear prestress over the rupture area. We also examine how the complexity of earthquake sequences, in terms of the variability of rupture size, differs with the efficiency of dynamic weakening. We study these behaviors in the context of simulations of sequences of earthquakes and slow slip, which allow the pre-stress conditions before earthquakes to be set by the loading conditions, evolving fault shear resistance (including weakening and healing), and stress redistribution by prior slip, as would occur on natural faults. Moreover, our simulations resolve the spontaneous nucleation process with the natural acceleration of slow unsteady slip prior to dynamic rupture. The constitutive relations for the evolving fault resistance and healing adopted in our models have been formulated as a result of a large body of laboratory, field and theoretical work (e.g Sibson, 1973; Dieterich, 1979; Ruina, 1983; Rice, 2006; Wibberley et al., 2008; Di Toro et al., 2011). Indeed, laboratory experiments of fault shear resistance at both slow and fast slip rates have been indispensable for our understanding of fault behavior and for formulating fault models such as the ones used in this study. The modelling allows us to examine the implications of the laboratory-derived constitutive behaviors for the larger-scale behavior of faults, and we compare our inferences of average shear prestress from relatively large-scale finite-fault modeling to field measurements of crustal stresses acting on mature faults and small-scale laboratory measurements of the shear resistance of typical fault materials.

152 **2 Building on laboratory constraints to model larger-scale fault be-**
153 **havior**

154 Laboratory experiments have been instrumental for exploring aspects of fault re-
155 sistance during both slow and fast sliding (10^{-9} m/s - 1 m/s, Figure 1). Experiments
156 with slow sliding velocities ($< 10^{-3}$ m/s) are critical for formulating fault constitutive
157 laws that form the basis for understanding the nucleation of earthquake ruptures. High-
158 velocity laboratory friction experiments have demonstrated enhanced dynamic weaken-
159 ing of faults and elucidated a range of mechanisms by which this dynamic weakening can
160 occur (e.g. Han et al., 2007; Wibberley et al., 2008; Goldsby & Tullis, 2011; Di Toro et
161 al., 2011; Faulkner et al., 2011; De Paola et al., 2015; Acosta et al., 2018). Most slow-
162 and high-velocity experiments measure or infer the relevant quantities - slip, slip rate,
163 shear stress etc - averaged over the sample and examine the evolution of shear resistance
164 corresponding to a particular history of loading, such as imposed variations in the dis-
165 placement rate of the loading piston, and the particular fault conditions (normal stress,
166 temperature, pore fluid pressure, etc.). Some experimental studies imposed the expected
167 sliding motion during earthquakes in order to directly relate laboratory stress measure-
168 ments to seismological quantities, such as static stress drop and breakdown energy (e.g.
169 Sone & Shimamoto, 2009; Fukuyama & Mizoguchi, 2010; Nielsen et al., 2016).

170 To understand the full implications of the evolution of shear resistance measured
171 in small-scale experiments for slip at larger scales along natural faults, they are synthe-
172 sized into mathematical formulations and used in numerical modeling, for the following
173 reasons. During slipping events on a finite fault over scales of tens of meters to kilome-
174 tres - much larger than the experimental scale - the fault does not slip uniformly with
175 a predetermined slip-rate history. Rather, the slip event initiates on a portion of the fault
176 and then spreads along the fault, with varying slip-rate histories and final slips at dif-
177 ferent points along the fault. This is captured in inversions of large earthquakes (e.g. Heaton,
178 1990; Simons et al., 2011; Ye et al., 2016a; Tinti et al., 2016) and, to a degree, in larger-

scale experiments, sometimes involving analog materials (Lu et al., 2010; McLaskey et al., 2014; Svetlizky & Fineberg, 2014; Yamashita et al., 2015; Rubino et al., 2017). In the process, the slip (1) transfers stress to the more locked portions of the fault and (2) enters portions of the fault with different conditions - such as levels of shear pre-stress, pore fluid pressure, etc - and potentially different friction and hydraulic properties. Hence the resulting coupled evolution of shear resistance and slip rate at different locations on the fault is often quite different and, through stress transfer, strongly dependent on the entire slip process at all locations throughout the rupture. These nonlinear and often dynamic feedback processes on the scales of tens of meters to kilometers can currently be only captured through numerical modeling.

Many numerical models of earthquake source processes utilize insight from laboratory experiments that indicate that the resistance to shear τ along a fault depends on the sliding rate V and the quality and/or lifetime of the local contacts, typically parameterized by a state variable θ with units of time, as well as on the effective normal stress $\bar{\sigma} = \sigma - p$ acting on the fault, with σ being the normal stress and p being the pore fluid pressure localized within the shearing layer (e.g. Dieterich, 1979; Marone, 1998). For continuum problems involving frictional sliding, the motion within the continuum is governed by the balance of linear momentum, subject to the boundary condition that tractions are given by the constitutive law of the interface. For frictional sliding without changes in the elastodynamic normal stress σ , which is the case considered in this work, the boundary condition reduces to the shear stress being equal to the shear resistance on the interface ($y = 0$):

$$\begin{aligned}\tau_{\text{stress}}(x, y = 0, z; t) &= \tau_{\text{resistance}}(x, y = 0, z; t) \\ &= f(V, \theta)(\sigma - p).\end{aligned}\quad (1)$$

201 An important concept in the rate-and-state formulation of the friction coefficient $f(V, \theta)$
 202 is that the friction coefficient is not a fixed property of the interface but evolves over time,
 203 facilitating the time-dependent changes of shear resistance and hence shear stress along
 204 the fault during shear.

205 The most commonly used formulation of rate-and-state laws is the Dieterich-Ruina
 206 formulation (Dieterich, 1979; Ruina, 1983):

$$f(V, \theta) = \left[f_* + a \ln \frac{V}{V_*} + b \ln \frac{\theta V_*}{D_{\text{RS}}} \right], \quad (2)$$

207 where f_* is a reference steady-state friction coefficient at the reference sliding rate V_* ,
 208 D_{RS} is the characteristic slip distance, and a and b are the direct effect and evolution
 209 effect parameters, respectively. Our fault models are governed by a form of the laboratory-
 210 derived Dieterich-Ruina rate-and-state friction law regularized for zero and negative slip
 211 rates (Lapusta et al., 2000; Noda & Lapusta, 2010). The evolution of the state variable
 212 can be described by various evolution laws; we employ the aging law (Ruina, 1983):

$$\dot{\theta} = 1 - \frac{V\theta}{D_{\text{RS}}}, \quad (3)$$

213 which describes evolution during sliding as well as time-dependent healing in near-stationary
 214 contact. In our models, the shear resistance and shear stress also change due to the evo-
 215 lution of pore fluid pressure p .

216 We conduct numerical simulations following the methodological developments of
 217 Lapusta et al. (2000), Noda and Lapusta (2010) and Lambert et al. (2021) in order to
 218 solve the elastodynamic equations of motion with the fault boundary conditions, includ-
 219 ing the evolution of pore fluid pressure and temperature on the fault coupled with off-
 220 fault diffusion. The simulations solve for mode III slip on a 1-D fault embedded into a
 221 2-D uniform, isotropic, elastic medium (Figure 2). The potential types of slip on the fault
 222 include sequences of earthquakes and aseismic slip (SEAS) and they are simulated in their

223 entirety, including the nucleation process, dynamic rupture propagation, postseismic slip
224 that follows the event, and interseismic period between seismic events that can last up
225 to tens or hundreds of years and host steady and transient slow slip (Figure 2).

226 The simulated fault in our models contains a 24-km-long segment with velocity-
227 weakening (VW) frictional properties where earthquake ruptures may nucleate and prop-
228 agate, surrounded by velocity-strengthening (VS) segments that inhibit rupture nucle-
229 ation and propagation. Our simulations include enhanced dynamic weakening due to the
230 thermal pressurization of pore fluids, which occurs when pore fluids within the fault shear-
231 ing layer heat up and pressurize during dynamic rupture, reducing the effective normal
232 stress and shear resistance (Sibson, 1973; Rice, 2006; Noda & Lapusta, 2010). Thermal
233 pressurization is one potential mechanism for enhanced weakening; qualitatively simi-
234 lar results should hold for models with other types of enhanced dynamic weakening. We
235 follow the thermal pressurization formulation of Noda and Lapusta (2010) (Supplemen-
236 tary Materials). We approximate the effects of off-fault yielding by employing a limit on
237 the slip velocity $V_{\max} = 15$ m/s, which is motivated by detailed dynamic rupture sim-
238 ulations with off-fault yielding (Andrews, 2004) and discussed in detail in Lambert et
239 al. (2021).

240 For the purpose of comparing local frictional behavior with the average prestress
241 for dynamic ruptures of varying sizes, we focus this study on simulated ruptures that ar-
242 rest within the VW region, where the friction properties are uniform with a quasi-static
243 reference friction of 0.6, consistent with many materials exhibiting VW behavior in lab-
244 oratory experiments (Ikari et al., 2011). We examine the evolution of the apparent fric-
245 tion coefficient, or the ratio of the current shear stress τ to the interseismic drained ef-
246 fective normal stress ($\sigma - p_{\text{int}}$), where p_{int} is the interseismic drained value of the pore
247 pressure. The term "drained" refers to the effective stress with ambient pore pressure
248 unaffected by slip processes such as dilatancy, compaction, or thermal pressurization. The
249 values used for the direct and evolution effect parameters, a and b respectively, within

the VW region are consistent with typical laboratory values (Tables 1-3; Blanpied et al., 1991, 1995; Marone, 1998). Within the VS regions, we use higher values of the direct effect a in order to more efficiently stop VW-region-spanning ruptures, which helps to maintain a reasonable domain size for computational expense. The properties of the VS regions should not appreciably alter the conclusions of this work, as we focus on the average stress measures for "partial" ruptures that are arrested predominantly in the VW region. The properties of larger ruptures that span the entire VW region and that arrest in the fault regions with VS properties are more sensitive to the VS properties, as discussed in Perry et al. (2020).

We examine fault models with varying levels of ambient fluid overpressure in terms of the effective normal stress, as well as varying degrees of efficiency in enhanced weakening due to thermal pressurization. The parameter values we have chosen (Tables 1-3) are motivated by prior studies that have reproduced a range of seismological observations as well as low-stress, low-heat operation of mature faults (Perry et al., 2020; Lambert et al., 2021). The parameter values also facilitate our goal of examining ruptures in fault models with a range of efficiency in enhanced dynamic weakening. We refer to the weakening behavior of fault models as being mild, moderate or efficient in comparison to the underlying weakening of the standard rate-and-state friction. This can be approximately quantified as the difference between the steady-state frictional resistance at the plate rate and seismic slip rates, equal to $(\sigma - p_{\text{int}})(b - a) \ln(V_{\text{seis}}/V_{\text{pl}})$, which corresponds to about 10% times the interseismic effective normal stress for $V_{\text{seis}} = 1$ m/s. Mild weakening corresponds to additional dynamic weakening comparable to that of standard rate-and-state friction (e.g. Fault model TP 1 in Table 2) and efficient corresponds to weakening by 70 – 100% of the prestress, all the way to near-zero shear resistance during seismic slip. Moderate weakening refers to the regime in between (e.g. Fault models TP 2-4 in Table 2).

We define the beginning and end of dynamic rupture, t_{ini} and t_{fin} respectively, as well as the ruptured area Ω , using a slip velocity threshold ($V_{\text{thresh}} = 0.01 \text{ m/s}$) for seismic slip, based on previous studies (Perry et al., 2020; Lambert et al., 2021). Note that t_{ini} and t_{fin} refer to the beginning and end of the entire rupture event, which starts when one location on the fault reaches the threshold velocity and ends when all points on the fault drop below the threshold velocity. In the following, we use "rupture" to refer to such dynamic slip events, unless noted otherwise. Further description of the numerical methodology can be found in the Supplementary Materials.

3 Evolution of local slip and shear resistance and notions of failure

Our simulations capture the evolution of motion and shear stress across the fault over sequences of earthquakes spanning several thousands of years (Figure 2C). The initial distributions of shear stress and other quantities such as the slip rate are assumed to be uniform along most of the VW region of the fault at the start of our simulations, other than a small region of initially high prestress near the VW-VS boundary to nucleate the first rupture in the earthquake sequence. The distributions of shear stress and slip along the fault evolve to become highly variable throughout periods of fast earthquake-producing slip as well as slow aseismic slip and fault locking. Below we review how the rate-and-state friction framework allows the model to represent creeping, locked, and seismically slipping fault areas as well as transitions between these different styles of slip, a key feature of SEAS simulations (e.g Rice, 1993; Lapusta & Rice, 2003; T. Chen & Lapusta, 2009; Wu & Chen, 2014; Michel et al., 2017; Cattania, 2019; Erickson et al., 2020).

During dynamic rupture, the evolution of slip rate and shear stress can be particularly complex and variable along the fault. At points where individual ruptures nucleate, the slip rate gradually accelerates towards seismic slip rates and shear stress at the beginning of rupture, t_{ini} , is relatively high, with the apparent friction coefficient $\tau/(\sigma - p_{\text{int}})$ close to the quasi-static reference friction of 0.6. As seismic slip rates are reached,

Accepted Article

302 $\tau/(\sigma - p_{\text{int}})$ drops substantially due to thermal pressurization of pore fluids in a man-
303 ner qualitatively consistent with the enhanced dynamic weakening observed in high-velocity
304 laboratory friction experiments (Figure 2H). The evolution of slip rate and shear stress
305 outside of the nucleation region is even more complicated: The shear stress at t_{ini} , prior
306 to the arrival of the rupture front, can be much lower than the shear stress levels where
307 the rupture nucleates, then increases to a higher peak shear stress (set by the balance
308 between the dynamic stress concentration at the rupture front due to inertial effects and
309 peak shear resistance due to interseismic fault healing and the rate-and-state direct ef-
310 fect), and then decreases due to weakening with seismic slip (Figure 2H vs. I). Consis-
311 tently, the slip rate rapidly increases to seismic values at the beginning of slip and then
312 decreases, as in a typical Yoffe-like behavior for dynamic ruptures (Figure 2G; e.g Tinti
313 et al., 2005). Thus, even with the uniform normal stress and uniform parameters of the
314 assumed friction and pore pressure equations within the seismogenic VW region, the pre-
315 stress conditions throughout the rupture area can be highly variable and, in part, sub-
316 stantially different between regions of rupture nucleation and rupture propagation (Rice,
317 1993; Lapusta & Rice, 2003; Schmitt et al., 2015; Wu & Chen, 2014; Galis et al., 2017;
318 Barbot, 2019; Cattania, 2019).

319 Note that the peak shear stress during dynamic rupture of fault locations outside
320 the nucleation zone can correspond to much higher apparent friction coefficient (e.g., 0.95
321 in Figure 2I) than the reference friction coefficient ($f_* = 0.6$ in this study). This is due
322 to both the direct effect at the rupture tip and the high, interseismically "healed" value
323 of the state variable θ , as discussed in Lambert and Lapusta (2020) and the Supplemen-
324 tary Materials (equation S3). As follows from the first line of equation S3, the difference
325 between the peak friction coefficient and f_* due to the direct effect of $a \ln(V_{\text{peak}}/V_*)$ would
326 be 0.14 to 0.16 for $V_{\text{peak}} = 1$ to 10 m/s and other parameters of our model, with the
327 rest due to the much larger value of the "healed" state variable than that for sliding at
328 the reference sliding rate.

The local evolution of shear stress throughout the VW seismogenic zone differs among points based on the long-term history of motion, including both local slip as well as slip across the entire fault. For example, a point at the center of the VW region ($z = 0$ km) of one of our simulations (fault model TP 3 in Table 2, as shown in Figure 2C) experiences substantial slip only during the largest earthquake ruptures that span the entire VW domain, resulting in a relatively simple and quasi-repetitive pattern of stress accumulation and weakening over sequences of earthquakes (Figure 3A & C). In contrast, another point in the VW region closer to the VS boundary ($z = -9.6$ km) experiences different amounts of slip during dynamic ruptures of varying size, resulting in a more complicated evolution of shear stress with accumulating slip (Figure 3B & D).

In between individual earthquakes, the VS regions of the fault creep (i.e., slowly slip) with the slip rate close to the prescribed tectonic plate rate, due to that rate being imposed on the fault areas nearby, with occasional quasi-static accelerations due to post-seismic slip (Figure 4, left column). The creep penetrates into the VW regions nearby, creating fault areas prone to earthquake nucleation (Lapusta & Rice, 2003; Jiang & Lapusta, 2016; Michel et al., 2017) (Figure 4, right column). These points of the VW region close to the VS region (within one or so nucleation length) are reloaded due to creep and post-seismic slip from previous rupture within the VS regions. The loading rate at these points near the VS-VW boundary varies over time depending on the rate of motion in the VS region, which in turn depends on the previous history of co-seismic slip during dynamic ruptures in the VW region.

The slip rate and apparent friction at points close to the VW-VS boundary are typically brought to near steady conditions around the loading plate rate, however both exhibit small oscillations as these points continue to be loaded by creep in the VS region, resulting in further acceleration, slip and weakening, and thus the transmission of stress further into the VW region until a sufficiently large area is loaded to sustain rupture nucleation and acceleration to seismic slip rates (Figure 4E-G). This oscillatory behavior

is consistent with predictions from the stability analysis of a single degree-of-freedom spring-slider undergoing frictional slip, where the amplitude of the oscillations is expected to grow as the spring stiffness decreases below a critical stiffness value (Gu et al., 1984). The effective stiffness of the slipping fault zone in a continuum model is inversely proportional to the slipping zone size (Rice & Ruina, 1983), decreasing with the increasing slipping region. Note that this rate-and-state nucleation process has been used to explain the period-dependent response of microseismicity to periodic stress perturbations in Nepal, where seismicity shows significant variations in response to annual monsoon-induced stress variations but not to semidiurnal tidal stresses of the same magnitude (Ader et al., 2014).

In contrast, much of the VW region further away from the VS regions is essentially locked, which is expressed in the rate-and-state formulation as sliding at very low, but still non-zero, slip rates that are many orders of magnitude smaller than the loading rate (Figure 5A-B). This differential motion between the VS and VW regions loads points in the VW region (Figure 5C-D), gradually increasing shear stress there (e.g., between 700 and 800 years in Figure 5C). Note that the interseismic stressing rate is higher at locations closer to the creeping regions than further away from it (Figures 5C vs. 5D vs. 4F), as one would expect (Rice, 1993; Lapusta & Rice, 2003; Wu & Chen, 2014; Herrendörfer et al., 2015; Michel et al., 2017; Cattania, 2019). At the same time, the essentially locked points within the VW region experience time-dependent healing of the local shear resistance encapsulated in the increase of the state variable θ (Figure 5E-F). One of the manifestations of this healing is that larger interseismic increases in the state variable generally lead to higher peak shear stress during dynamic rupture propagation (Lambert & Lapusta, 2020). Despite the increase in the state variable, its value is far below the steady-state one for the very low interseismic slip rates, consistent with continuing healing prior to dynamic rupture (Figure 5G-H). Depending on whether the local shear stressing rate (which increases the shear stress τ on the left of equation 1) is larger or smaller than the rate of healing (expressed by the last, θ term on the right hand side of equa-

384 tion 2), the local slip rate (that enters the second term of equation 2) increases (as be-
385 tween 700 and 800 years in Figure 5A) or decreases, i.e., the fault is accelerating towards
386 failure or becomes even more locked. However, most of the locked points of the fault never
387 accelerate close to failure interseismically; rather, they fail due to stress concentrations
388 from dynamic events, seen as vertical lines in Figure 5C-D.

389 We note that healing on natural faults, in the presence of fluids and depth-dependent
390 elevated temperatures, can be affected by a number of mechanisms that are not captured
391 by the basic state evolution equation (Yasuhsara et al., 2005; Tenthorey & Cox, 2006; J. Chen
392 et al., 2015a, 2015b). Furthermore, different and more involved formulations of the state
393 evolution law exist, e.g. the slip law and various composite laws (Ruina, 1983; Perrin et
394 al., 1995; Kato & Tullis, 2001), some of which provide a better (although still imperfect)
395 match to laboratory experiments (Bhattacharya et al., 2015). Note that aging and slip
396 laws resulted in qualitatively similar results for simulations of repeating earthquake se-
397 quences (T. Chen & Lapusta, 2019). Exploring the behavior of our models with differ-
398 ent state evolution laws and incorporating more realistic healing into shear resistance
399 formulations and numerical modelling is an important goal for future work. This can be
400 done by modifying the evolution of the state variable θ or adding other state variables
401 that would encode healing. Yet, qualitatively, additional healing mechanisms would have
402 similar effects on the simulations as the current rate-and-state healing, in that the heal-
403 ing would modify the peak shear resistance and the subsequent evolution of the resis-
404 tance based on the interseismic fault state, potentially further amplifying differences in
405 shear resistance evolution for different points along the fault (e.g., nucleation points vs.
406 locked points) that our simulations already highlight.

407 The presence of time-dependent healing as well as persistent, potentially unper-
408 ceivable, slow (quasi-static) motion and its acceleration under variable levels of shear stress
409 illustrate how the concepts of failure, and hence strength, are not easily defined for fric-
410 tional sliding. For realistic frictional interfaces, the precise value of a static friction co-

efficient is ill-defined, since no interface loaded in shear is perfectly static; rather creep processes occur at slow, unperceivable slip rates at any level of shear loading (Dieterich & Kilgore, 1994; Bhattacharya et al., 2017) and/or over parts of the contacting interfaces (Rubinstein et al., 2004, 2006; Ben-David et al., 2010). Hence the transition from locked interfaces to detectable slip is always a gradual process (although it may be occurring faster than the time scales of interest/observation in many applications). This reality is reflected in lab-derived fault constitutive relations such as rate-and-state friction. Since failure typically refers to the presence of irreversible or inelastic deformation, frictional interfaces may be considered failing under any style or rate of motion, be it during slow steady sliding, transient slow slip, or dynamic rupture. Therefore, any meaningful notion of strength first requires definition of the failure of interest, e.g., reaching seismic slip rates of the order of 1 m/s. Without such explicit definition, failure is then implicitly defined as transition from locked to slipping and corresponds to sliding with a detectable velocity; for laboratory experiments or observational studies, this would imply that whether the interface is locked or slipping depends on the instrumental precision for detectable motion.

In this study, we would like to compare the shear stress values required for aseismic slip nucleation and for dynamic rupture propagation. During spontaneous aseismic slip nucleation, the slip rates evolve from very low to seismic, passing in the process through the slip rate equal to the tectonic loading rate V_{pl} . In the standard rate-and-state friction, at each fixed sliding rate V , the friction coefficient eventually evolves to a steady-state value $f_{ss}(V)$ (equation S2; for very small slip rates, the regularized formulation of equation S5 needs to be considered). Under slow loading, aseismic earthquake nucleation on a finite fault is typically a gradual process, with many points within the nucleation zone being close to the steady state (Figure 4; Rubin & Ampuero, 2005; Kaneko & Lapusta, 2008). While the steady-state values of friction depend on the sliding rate, the dependence is relatively minor at the low, quasi-static slip rates between the plate rate of approximately 10^{-9} m/s and sub-seismic slip rates of $< 10^{-3}$ m/s (Figure 1) which

439 are relevant for fault creep and earthquake nucleation, and for which the standard rate-
 440 and-state formulation is (approximately) valid. The product of this collection of steady-
 441 state quasi-static friction coefficients and the interseismic drained effective stress gives
 442 the shear resistance of faults at sustained slow sliding rates, which we call the *steady-*
 443 *state quasi-static fault shear resistance* (referred to in short as local SSQS shear resis-
 444 tance). As the representative value of such local SSQS shear resistance, we choose the
 445 shear resistance of the fault steadily creeping at the prescribed long-term tectonic plate
 446 rate V_{pl} (which the fault would have long-term if it were slipping stably), with the in-
 447 terseismic drained value of the pore pressure p_{int} :

$$\tau_{ss}^{V_{\text{pl}}}(z, t) = (\sigma - p_{\text{int}}) f_{ss}(V_{\text{pl}}) \quad (4)$$

448 In our models, $\tau_{ss}^{V_{\text{pl}}} / (\sigma - p_{\text{int}}) = 0.63$ within the VW region. Note that choosing V_* in-
 449 stead of V_{pl} would result in a similar value of $\tau_{ss}^{V_{\text{pl}}} / (\sigma - p_{\text{int}}) = f_* = 0.6$.

450 In the following section, we compare this representative value of local SSQS shear
 451 resistance to the spatial distribution of shear stress prior to dynamic ruptures in our sim-
 452 ulations. Note that the local SSQS shear resistance is similar to what is typically viewed
 453 as "frictional fault strength" in the sense of Byerlee (1978), i.e., this is the resistance that
 454 needs to be met for noticeable quasi-static slip with the loading rate or another refer-
 455 ence rate.

456 4 Larger ruptures associated with lower shear prestress over the rup- 457 ture scale but higher prestress over smaller scales near nucleation

458 The interseismic periods in between individual earthquake ruptures in our simu-
 459 lations vary from months to decades, depending on the size of the rupture and the stress
 460 state resulting from the history of prior slip along the fault. Our earthquake sequence
 461 simulations produce a wide variety of rupture sizes due to heterogeneous prestress con-
 462 ditions along the fault that spontaneously arise in our models.

Let us consider the evolution of slip and shear stress in representative simulated spontaneous ruptures of increasing sizes within the same simulation (Figure 6). Over sequences of rupture events, the shear stress conditions prior to and after individual dynamic ruptures become spatially heterogeneous. This stress heterogeneity is due in part to the history of spatially variable slip and local static stress drop produced in previous ruptures, as well as stress relaxation and redistribution due to aseismic slip. In addition, while our simulated fault models are loaded by a constant long-term loading rate of V_{pl} , the effective loading conditions along the fault interface vary in space and time due to differences in slip rate along the fault. Ruptures nucleate preferentially in regions with the highest shear prestress, which in our models occur near the creeping regions as discussed in section 3 (Figure 6; Lapusta et al., 2000; Michel et al., 2017; Barbot, 2019). The ruptures then propagate into the less stressed areas of the fault. Put another way, the average prestress over the nucleation region is higher than the average prestress over the entire ruptured region (Figure 7A vs. B), as we quantify in the following.

We compute the average shear prestress right before a dynamic rupture event over the entire future rupture area (which we do as post-processing of data in our simulation). We also compute the average shear prestress over the slow-slip nucleation zone, which we call the *nucleation stress*. We compare these average shear stress measures with the *local steady-state quasi-static (SSQS) fault shear resistance* $\tau_{ss}^{V_{\text{pl}}}$, which is related to the local fault constitutive properties during slow slip and given by equation 4.

Averaging of spatially variable stress fields can be done in several different ways (Noda & Lapusta, 2012; Noda et al., 2013). The simplest definition of the average shear prestress over the rupture region Ω is the spatially averaged prestress τ_{ini}^A acting in the overall slip direction at the beginning of the rupture t_{ini} , given by:

$$\tau_{\text{ini}}^A = \frac{\int_{\Omega} \tau(z, t_{\text{ini}}) dz}{\int_{\Omega} dz}. \quad (5)$$

We can similarly define the spatially averaged nucleation stress τ_{nucl}^A within the nucleation region. We define the nucleation region to be the fault segment between the expanding stress fronts at the initiation of dynamic rupture; the size of the nucleation regions in our simulations is comparable to the theoretical nucleation size estimate h_{RA}^* of Rubin and Ampuero (2005) (equation S6, Figure S1).

Not surprisingly and consistent with prior studies, we find that the spatially averaged nucleation stress τ_{nucl}^A for our simulated ruptures is comparable to the local SSQS shear resistance $\tau_{ss}^{V_{p1}}$ (Figure 7A; Perry et al., 2020; Lambert et al., 2021). As a consequence, it does not significantly depend on the ultimate rupture size or slip. Since the nucleation stress here is computed at the beginning of dynamic rupture, it is then the shear stress within the nucleation zone at the end of the nucleation, when parts of the zone slip with near-dynamic slip rates approaching 10^{-2} m/s. That is why the nucleation stress is systematically slightly lower than the local SSQS shear resistance defined as the steady-state shear resistance to slip with the (lower) plate rate. The difference between the nucleation stress and local SSQS shear resistance could be more substantial if dynamic weakening were efficient enough to affect some portion of the earthquake nucleation region (Segall & Rice, 2006).

In contrast, the spatially averaged prestress over the entire ruptured area τ_{ini}^A tends to decrease with the rupture size and increasingly deviate from the local SSQS shear resistance and nucleation stress for increasingly efficient dynamic weakening (Figures 6 & 7B). Such behavior is also true for another average prestress measure, the energy-based average prestress $\bar{\tau}_{\text{ini}}^E$ (Noda & Lapusta, 2012), which is the average shear prestress weighted by the final slip of the rupture, and hence represents the average prestress associated with the potency of the impending rupture:

$$\bar{\tau}_{\text{ini}}^E = \frac{\int_{\Omega} \tau(z, t_{\text{ini}}) \delta_{\text{fin}}(z) dz}{\int_{\Omega} \delta_{\text{fin}}(z) dz} \quad (6)$$

where $\delta_{\text{fin}}(z) = \delta(z, t_{\text{fin}}) - \delta(z, t_{\text{ini}})$ is the final local slip accrued in the rupture. We denote $\bar{\tau}^E$ with a bar as it not only represents an average over space but also requires knowledge of the final slip of the rupture. $\bar{\tau}_{\text{ini}}^E$ differs from the spatially-averaged pre-stress τ_{ini}^A over the rupture area when the resulting slip distribution is not uniform. We find that $\bar{\tau}_{\text{ini}}^E$ and τ_{ini}^A for our simulated ruptures are comparable and vary similarly with the rupture size and efficiency of dynamic weakening, with the values of $\bar{\tau}_{\text{ini}}^E$ being slightly larger (Figure S2).

For the range of simulated rupture sizes considered, we find that the decrease in average shear pre-stress with increasing rupture size in our 2-D models with 1-D faults is consistent with a power-law relationship between the average shear pre-stress nondimensionalized by the representative local SSQS shear resistance and the ratio of the rupture length λ_{rupt} to nucleation size h_{RA}^* (Figure 7C):

$$\frac{\tau_{\text{ini}}^A}{\tau_{ss}^{V_{\text{pl}}}^A} = c_2 - c_1 \log_{10} \left[\frac{\lambda_{\text{rupt}}}{h_{\text{RA}}^*} \right], \quad (7)$$

where c_1 and c_2 are fit parameters (Table 4). We find that c_2 is comparable to unity for all our simulations (Table 4), while c_1 depends on the efficiency of weakening in each simulation, increasing by about a factor of 5 from 0.07 in our fault models with no enhanced weakening (RS1 and 2) to around 0.3 in models with moderate enhanced weakening (TP3 and 4). Thus, for a decade increase in rupture length λ_{rupt} with respect to nucleation size h_{RA}^* , the decrease in the spatially averaged pre-stress with increasing rupture size differs by a factor of 5 between our models with no to moderately efficient enhanced dynamic weakening. We find comparable results for the energy-based pre-stress $\bar{\tau}_{\text{ini}}^E$ (equations S9-10, Figure S3 and Table S1).

The finding that larger ruptures are associated with smaller average shear pre-stress over the ruptured area may appear counterintuitive. Why do smaller ruptures not become larger if they are more favorably prestressed? To understand this behavior, let us consider the pre-stress averaged over several fixed scales around the nucleation region for

531 ruptures of different sizes. We locate the VW-VS boundary next to which each of our
532 simulated ruptures nucleate and average the prestress along the VW region over fixed
533 distances (1, 2, 4, 8, 12 and 16 km) from the corresponding VW-VS boundary (Figure
534 8; shown for fault model TP4 from Table 2). While the spatially-averaged prestress over
535 the entire rupture length decreases with increasing rupture size, we see that the prestress
536 spatially-averaged over smaller fixed scales is generally higher for larger ruptures than
537 for smaller ruptures (Figure 8 warmer vs cooler colored triangles). For smaller ruptures,
538 the average shear stress over scales just larger than their total rupture length is lower
539 than the average prestress of larger ruptures with comparable length to the fixed aver-
540 aging scales (Figure 8, triangles below the circles). This confirms that the smaller rup-
541 tures arrest because the prestress conditions ahead of the rupture are too low to sustain
542 further rupture propagation. For larger ruptures, the average prestress levels at scales
543 smaller than their total rupture length are generally higher or comparable to the aver-
544 age prestress over smaller ruptures with the length comparable to the fixed averaging
545 scales (Figure 8, triangles above the circles). This finding suggests that larger ruptures
546 have higher, more favorable average prestress conditions at smaller scales compared to
547 smaller ruptures, which facilitates continued rupture propagation. Hence we find that
548 the shear prestress prior to our simulated ruptures of varying sizes self-organizes into a
549 spatial distribution of scale-dependent average shear stress that governs the rupture oc-
550 currence.

551 As discussed in Perry et al. (2020), the decrease in average prestress with increas-
552 ing rupture size can result in nearly magnitude-invariant static stress drops. Note that,
553 as the static stress drop for points throughout typical rupture propagation for our sim-
554 ulated ruptures with efficient enhanced dynamic weakening is lower than the static stress
555 drop within the nucleation region (Figure 2H vs I), the average static stress drop can de-
556 crease as the rupture length increases beyond the nucleation length (Figure S3; Ampuero
557 et al., 2006; Perry et al., 2020). The effect is more noticeable for the energy-based stress
558 drop which weights the local static stress drop by the local slip, but becomes less pro-

nounced for our simulated ruptures that are considerably larger than the nucleation length.
 We refer to these ruptures as having nearly magnitude-invariant static stress drops, since
 the variation of the stress drop with rupture size is relatively mild and would likely fall
 within the scatter and uncertainty of seismological observations (Allmann & Shearer, 2009;
 Ye et al., 2016b).

5 Role of dynamic stress transfers and motion-dependent local shear resistance

Such scale- and motion-dependent average fault shear prestress before ruptures results from two related and interacting factors. First, as dynamic rupture propagates, some of the released energy is carried by waves along the fault, creating a substantial stress concentration near the rupture tip that is a well-known feature of dynamic rupture (e.g., Freund, 1990). The stress concentration enables rupture propagation over regions where the prestress is lower than the local SSQS shear resistance, drawing the local shear stress up to the peak stress before the subsequent stress drop due to local weakening (black lines in Figure 6). The dynamic stress concentration increases with the rupture dimension and/or slip and thus allows larger ruptures to continue propagating over regions with lower, and hence less favorable, prestress conditions (Figure 6). This is illustrated in this work for largely crack-like ruptures that occur in the presented models with mild to moderate enhanced dynamic weakening (Lambert et al., 2021), but similar conclusions would be reached for pulse-like ruptures provided that they satisfy the observational constraint of magnitude-independent stress drops, which implies that ruptures with larger magnitudes would have larger average slip and hence larger stress concentrations. Note that a pulse-like rupture with the same or similar spatial distribution of the slip rate (and hence the same local slip) propagating along the fault would result in a similar stress concentration at the rupture tip regardless of the rupture length; however, in that scenario, pulses with larger rupture propagation lengths would have systematically lower static stress drops,

585 as the stress drops would be proportional to the (uniform) pulse slip divided by ever in-
586 creasing propagation lengths.

587 Second, the evolving local shear resistance substantially depends on both the prior
588 history of slip events on the fault through fault prestress and on the motion during the
589 current rupture event through dynamic stress transfers that add substantial time-dependent
590 loading. This pronounced dependence is due to strong coupling between the evolving mo-
591 tion and shear resistance, which is coupled to the resulting shear heating in the case of
592 thermally-activated weakening mechanisms like thermal pressurization. As a result, the
593 evolution of local slip rate and local shear resistance (1) significantly differs at different
594 fault locations of each rupture (despite uniform constitutive properties) and (2) signif-
595 icantly differs at the same fault location for different ruptures (Figures 2D-I and 6D-E).

596 These two factors create a substantial positive feedback, in which larger ruptures
597 with more slip generate larger stress concentrations, leading to faster and larger slip, which
598 dynamically causes more fault weakening, which in turn promotes more/faster slip, more
599 energy release, larger stress concentrations, and increasing rupture sizes.

600 The result that larger ruptures are associated with lower average prestress indicates
601 the need for increasingly less favorable stress conditions to arrest growing ruptures. For
602 a given rupture size, if the prestress ahead of the rupture is favorable, then the rupture
603 would continue to grow until it experiences sufficiently unfavorable prestress conditions,
604 thus lowering the overall average prestress. Alternatively, the rupture may be forcibly
605 arrested by other means such as strong geometric or rheological barriers. For example,
606 ruptures propagating over higher prestress conditions within the VW region can be ar-
607 rested by fault regions with VS properties; in those cases, the overall average prestress
608 conditions would depend on the properties of the VS regions (Perry et al., 2020). De-
609 tailed study of the implications of fault geometry and heterogeneity for rupture arrest
610 and the average stress conditions prior to rupture is an important topic for future work.

611 **6 Comparison of finite-fault modeling to single-degree-of-freedom rep-**
 612 **resentations**

613 As captured in field observations of natural earthquakes and reflected in our sim-
 614 ulations, sufficiently large earthquake ruptures nucleate on a subsection of the fault and
 615 then propagate through other sections of the fault. Capturing such space-dependent be-
 616 havior is typically called "finite-fault" modeling, in contrast to the point source that con-
 617 siders a spatially averaged representation of an event, as if it occurs at one "point". A
 618 typical numerical model of a point source is the single-degree-of-freedom system (SDOF)
 619 of a slider with friction pulled by a spring (e.g. Dieterich, 1979; Ruina, 1983; Rice & Ru-
 620 ina, 1983). Small-scale laboratory experiments often measure properties averaged over
 621 a sample and are typically modeled as a SDOF spring-slider systems.

622 The significant role of spatially varying prestress conditions and dynamic stress trans-
 623 fers during rupture propagation in determining the rupture behavior implies that cap-
 624 turing the finite-fault nature of the process is essential for determining the stress evo-
 625 lution characteristic of dynamic rupture. For example, several laboratory studies applied
 626 variable slip rates histories inferred from natural earthquakes to rock samples, measured
 627 the resulting shear resistance, and then related laboratory stress measurements to seis-
 628 mological source properties such as breakdown energy and stress drops (e.g. Sone & Shi-
 629 mamoto, 2009; Fukuyama & Mizoguchi, 2010; Nielsen et al., 2016). Such experiments
 630 have provided invaluable data about the local shear resistance of faults, specifically en-
 631 hanced dynamic weakening, that have informed theoretical and numerical modeling of
 632 finite faults (e.g. Zheng & Rice, 1998; Rice, 2006; Noda et al., 2009; Noda & Lapusta,
 633 2010; Dunham et al., 2011; Gabriel et al., 2012; Perry et al., 2020; Lambert et al., 2021),
 634 including the current study. However, the interpretation of such experiments needs to
 635 take into account their SDOF nature. For example, to improve alignment etc, the ex-
 636 periments often impose pre-sliding at slow slip rates (of the order of micron/s) prior to
 637 imitating seismic motion. That procedure results in the shear prestress before seismic

slip comparable to the local SSQS shear resistance (equation 4) and near steady-state values of the state variable, as appropriate for a location within a nucleation zone. In contrast, our simulations show that most points on a fault through which the rupture propagates have much lower shear prestress and much larger values of the state variable corresponding to well-healed fault (Figures 6 and 9B). Furthermore, the experiments often apply smoothed slip-rate histories obtained from finite-fault inversions, while the stress concentration at the tip of dynamic rupture makes the slip rate variation much more dramatic.

To illustrate the differences for the shear resistance evolution obtained with such experimental procedures versus the one from our simulated finite-fault models, let us compare the local fault behavior during one of our dynamic ruptures with a SDOF calculation. In the SDOF calculation, we use the same fault properties (equations 3, S4 and S7-8) and same parameter values as in the finite-fault VW regions but apply quasi-static presliding and modified, smoothed slip rates motivated by the laboratory procedures of Fukuyama and Mizoguchi (2010) (further details in Supplementary Materials). We conduct the comparison for two fault locations, one in the nucleation region and one within dynamic rupture propagation region (Figure 9). These SDOF calculations are successful at reproducing the presence of the enhanced dynamic weakening with slip as occurs during dynamic ruptures and generally capture the more moderate slip evolution and behavior of points within the nucleation region of our simulated dynamic ruptures. At the same time, the overall shear stress evolution during typical propagation of the dynamic rupture substantially differs from that of the SDOF calculation, with notable features including the low initial stress (which depends on prior slip history) relative to the SSQS shear resistance, the much more dramatic increase in shear stress associated with the dynamic rupture front (which arises due to the more healed fault coupled with the dynamic stress concentration), and the shear stress evolution at the end of slip (which depends on the final slip distribution over the entire finite fault) (Figure 9).

665 7 Implications for earthquake statistics

666 A notable feature of the scale dependence of average prestress before dynamic rup-
 667 ture is that, as an earthquake grows larger, the prestress needed for further propagation
 668 decreases (Figure 7B). In addition, the higher the weakening rate, the easier it should
 669 be for a rupture to have favorable prestress conditions to continue growing, rather than
 670 arresting as a smaller earthquake. Hence one could hypothesize that the more efficient
 671 the enhanced dynamic weakening, the smaller the complexity of the resulting earthquake
 672 sequences, with increasing representation of larger events at the expense of smaller events.

673 This is exactly what our modeling shows (Figure 10). The fault models with in-
 674 creasingly more efficient weakening produce earthquake sequences with increasingly fewer
 675 small events and decreasing b-values of the cumulative size distribution (Figure 10; de-
 676 tails for calculating seismic moment in the supplementary text). Fault models with even
 677 more efficient dynamic weakening than considered in this study, such as those that pro-
 678 duce sharp self-healing pulses, result in relatively simple earthquake sequences consist-
 679 ing of only large events (Lambert et al., 2021). The fault models governed by relatively
 680 mild to more moderate weakening as considered in this work develop a wider range of
 681 earthquake sizes, due to a feedback loop of more likely rupture arrest due to milder weak-
 682 ening creating stress heterogeneity that in turn makes rupture arrest more likely. This
 683 result is consistent with those of previous quasi-dynamic earthquake sequence simula-
 684 tions demonstrating complex earthquake sequences with higher b-values around 0.75 on
 685 faults governed by standard rate-and-state friction only and milder quasi-dynamic stress
 686 transfer, as well as relatively large fault lengths compared to the nucleation size, $\lambda_{\text{VW}}/h_{\text{RA}}^* >$
 687 100 (Cattania, 2019; Wu & Chen, 2014). Our results show b-values around 0.5 for fully
 688 dynamic simulations with instability ratios of $\lambda_{\text{VW}}/h_{\text{RA}}^* = 44$ and without enhanced
 689 dynamic weakening, which further decrease to 0.25 or so for the most efficient weaken-
 690 ing considered in this study. Note that simulations with higher instability ratios and even
 691 more efficient dynamic weakening than considered in this work, such as that consistent

with the propagation of sharp self-healing pulses, can result in only large earthquakes (Lambert et al., 2021), consistent with our observation of decreasing variability of rupture sizes for fault models with more efficient dynamic weakening, even in cases with relatively high instability ratios.

While the frequency-magnitude distribution of seismicity over relatively large regions, such as Northern or Southern California, is generally well-described by Gutenberg-Richter scaling with typical b-values near unity (Field et al., 2013), whether such scaling applies to individual fault segments and/or their immediate surroundings is a topic of active research (Wesnousky, 1994; Ishibe & Shimazaki, 2012; Kagan et al., 2012; Page & Felzer, 2015; Page & van der Elst, 2018; Field et al., 2017). Estimates of b-values associated with individual fault segments can exhibit considerable variability (e.g. between 0.5 and 1.5 along faults in California; Schorlemmer & Wiemer, 2005; Tormann et al., 2014), and are sensitive to a number of factors, including the magnitude of completeness of the relevant earthquake catalog and the choice of observation region and time window (Tormann et al., 2014; Page & Felzer, 2015; Ishibe & Shimazaki, 2012; Page & van der Elst, 2018). A number of studies suggest that the rate of large earthquakes on major faults, such as the San Andreas Fault, is elevated above what would be expected given typical Gutenberg-Richter scaling from smaller magnitude events (Schwartz & Coppersmith, 1984; Field et al., 2017). In particular, some mature fault segments that have historically hosted large earthquakes, such as the Cholame and Carrizo segments of the San Andreas Fault, exhibit substantial deviations from typical Gutenberg-Richter scaling, being nearly absent of small earthquakes (Sieh, 1978; Wesnousky, 1994; Bouchon & Karabulut, 2008; Hauksson et al., 2012; Jiang & Lapusta, 2016; Michailos et al., 2019). Our findings suggest that the paucity of microseismicity on such mature fault segments may indicate that they undergo substantial dynamic weakening during earthquakes ruptures.

717 8 Discussion

718 Our simulations reemphasize that the average shear prestress required for rupture
 719 propagation can be considerably lower than the average shear stress required for the rup-
 720 ture nucleation (Rice, 1993; Lapusta & Rice, 2003; Wu & Chen, 2014; Schmitt et al., 2015;
 721 Galis et al., 2017; Barbot, 2019; Cattania, 2019). This is because the quasi-static nucle-
 722 ation process is governed by relatively small stress changes and hence requires favorable
 723 prestress conditions - close to the local steady-state quasi-static shear resistance - to pro-
 724 ceed. In contrast, during dynamic rupture, the rupture front is driven by larger wave-
 725 mediated dynamic stress concentrations, which are more substantial for larger ruptures
 726 and facilitate rupture propagation over less favorably stressed regions, resulting in the
 727 spatially-averaged prestress over the ruptured area being much lower than the average
 728 local SSQS shear resistance. More efficient weakening facilitates larger dynamic stress
 729 changes at the rupture front, allowing propagation over even less favorable prestress con-
 730 ditions. Our results highlight the significance of heterogeneity in prestress, or shear re-
 731 sistance, for the nucleation and ultimate arrest of finite ruptures, even in fault models
 732 that have otherwise uniform material and confining properties.

733 The decrease in averaged prestress with rupture length can be interpreted as a de-
 734 crease in the average quasi-static friction coefficient $\tau_{\text{ini}}^A / (\sigma - p_{\text{int}})$ with rupture size (Fig-
 735 ure 7). The average quasi-static friction coefficients for ruptures on the scale of the nu-
 736 cleation size are consistent with the prescribed quasi-static reference friction coefficient
 737 near typical Byerlee values. However, as we average the prestress over larger rupture lengths,
 738 the average quasi-static friction coefficient can considerably decrease depending on the
 739 efficiency in weakening.

740 The presence of enhanced dynamic weakening draws the average shear stress along
 741 larger regions of the fault below the local SSQS consistent with earthquake nucleation,
 742 resulting in lower average shear stress conditions in terms of both the average prestress
 743 for larger ruptures and the average dynamic resistance associated with shear heating dur-

ing ruptures (Figure 11). The models presented in this study with mild-to-moderate enhanced weakening include considerable persistent fluid overpressurization to maintain low-heat, low-stress conditions with average dynamic shear resistance during seismic slip rates below 10 MPa; however the degree of fluid overpressure required to maintain low-heat conditions is less than that with comparable rate-and-state properties but no enhanced weakening. The presence of some enhanced dynamic weakening is also needed for persistently weak fault models due to chronic fluid overpressure in order to ensure that static stress drops are not too small, as they would otherwise be with low effective stress and small changes in the friction coefficient due to standard rate-and-state laws (Figures 11 and S3; Lambert et al., 2021). Fault models with more efficient dynamic weakening have been shown to be able to reproduce low-stress operation and reasonable static stress drops with quasi-static friction coefficients around Byerlee values and higher effective normal stress (e.g. ≥ 100 MPa; Noda et al., 2009; Dunham et al., 2011; Lambert et al., 2021). Earthquake sequence simulations of such fault models typically consist of only large ruptures (Lambert et al., 2021), consistent with the notion that large fault areas governed by efficient weakening maintain substantially lower average shear stresses than that required for nucleation. These findings further strengthen the conclusion of prior studies that enhanced dynamic weakening can help explain the discrepancy between laboratory values of (quasi-static) friction coefficients around 0.6 and geophysical inferences of low effective coefficients of friction (< 0.2), along with mild average static stress drops of 1 to 10 MPa, over fault areas that host large earthquakes (e.g Marone, 1998; Suppe, 2007; Allmann & Shearer, 2009; Noda et al., 2009; Dunham et al., 2011; Ikari et al., 2011; Gao & Wang, 2014; Ye et al., 2016b; Perry et al., 2020; Lambert et al., 2021).

The scale dependence of average prestress before ruptures can also be interpreted as a scale dependence of *average fault strength*, since the average prestress represents a measure of how much shear stress that fault region can hold before failing in a rupture. Given this interpretation, our simulations suggest that faults maintain lower average shear

772 stresses, and hence appear weaker (or understressed with respect to quasi-static failure),
773 at larger scales than at smaller scales. This interpretation is conceptually consistent with
774 laboratory measurements of scale-dependent yield stress for rocks and a number of en-
775 gineering materials, which demonstrate decreasing material strength with increasing scale
776 (Jaeger & Cook, 1976; Bandis et al., 1981; Greer et al., 2005; Pharr et al., 2010; Uchic
777 et al., 2004; Yamashita et al., 2015; Thom et al., 2017). Note that our larger simulated
778 ruptures, even with more efficient weakening, still require higher average shear stresses
779 over smaller scales in order to nucleate and grow. Thus the lower average prestress lev-
780 els that allow continued failure in dynamic ruptures at larger scales only become rele-
781 vant once the rupture event has already nucleated and sufficiently grown over smaller
782 scales. Hence, while the faults appear to be weaker on larger-scales, they are clearly not
783 truly so, in the sense that the "stronger" small scales have to fail quasi-statically before
784 the larger scales can fail dynamically, and that small-scale quasi-static strength can be
785 high everywhere on the fault. This consideration suggests that the critical stress con-
786 ditions for rupture occurrence are governed not by a single stress quantity but by a dis-
787 tribution of scale-dependent stress criteria for rupture nucleation and continued prop-
788 agation. An important implication of our findings is that the critical stress for earthquake
789 occurrence may not be governed by a simple condition such as a certain level of Coulomb
790 stress. Given our findings, in order to reason about the stress conditions critical for a
791 rupture to occur, it is important to consider both the size of the rupture and the weak-
792 ening behavior, and hence the style of motion, that may occur throughout rupture prop-
793 agation.

794 The scale dependence of fault material strength has also been hypothesized to ex-
795 plain the measured scaling of roughness on natural fault surfaces (Brodsky et al., 2016).
796 Dynamic rupture simulations on geometrically irregular faults motivated by such rough-
797 ness measurements have indicated an additional contribution to fault shear resistance
798 arising from roughness drag during rupture propagation (Fang & Dunham, 2013). Fur-

ther examination of the scale dependence of average shear resistance across faults including realistic fault geometry is an important topic for future work.

A common assumption when considering the average motion along a fault in relation to a SDOF system is that the shear prestress over the entire ruptured area must be near the average local static (or quasi-static) strength, comparable to the SSQS shear resistance discussed in this study. Our results reemphasize that the assumption is not necessarily valid for finite ruptures; moreover, faults with enhanced dynamic weakening and history of large earthquake ruptures would, in fact, be expected to have low average shear stress over large enough scales. At the same time, the state of stress needs to be heterogeneous, with the average stresses over small scales (comparable to earthquake nucleation) being close to the (much higher) local SSQS shear resistance in some places. Thus, while individual measurements of low resolved shear stress onto a fault may suggest that those locations appear to not be critically stressed for quasi-static failure, those regions, and much of the fault, may be sufficiently stressed to sustain dynamic rupture propagation and hence large earthquake ruptures.

In addition, our findings suggest that inferences of stress levels on faults may differ if they are obtained over different scales or influenced by different rupture processes. For example, low-stress conditions on mature faults from observations of low heat flow may not only represent average shear stress conditions over large fault segments as a whole but also be dominated by low dynamic resistance during fast slip, whereas averages over smaller scales would be expected to reflect the heterogeneity of the underlying prestress distribution, as perhaps reflected in varying stress rotations inferred over scales of tens of kilometers (Hardebeck & Hauksson, 1999, 2001; Hardebeck, 2015). This assertion fits with the notion of "strong" intraplate faults where crustal stress measurements suggest stress levels commensurate with incipient failure on faults with Byerlee friction (Townend & Zoback, 2000). In these regions, the smaller intraplate faults require higher prestress

825 levels across the entirety of the fault surface not only for nucleation, but also propagation.
826

827 Our modeling shows that increasingly efficient dynamic weakening leads to different
828 earthquake statistics, with fewer small events and increasing number of large events.
829 Another factor that can significantly affect the ability of earthquake ruptures to prop-
830 agate is fault heterogeneity, including variations in the rate-and-state frictional proper-
831 ties, effective normal stress, and fault roughness (e.g. Hillers et al., 2006, 2007; Ampuero
832 et al., 2006; Schaal & Lapusta, 2019; Heimisson, 2020; Cattania & Segall, 2021). Some
833 dynamic heterogeneity in shear stress spontaneously develops in our simulations, lead-
834 ing to a broad distribution of event sizes for cases with mild to moderate enhanced dy-
835 namic weakening. Our findings suggest that the effects of pre-existing types of fault het-
836 erogeneity need to be considered with respect to the size of the rupture and weakening
837 behavior on the fault. For example, faults that experience more substantial weakening
838 would require the presence of larger amplitudes of small-wavelength heterogeneity in shear
839 stress or resistance to produce small events. Examining the relationship between earth-
840 quake sequence complexity and varying levels of fault heterogeneity and enhanced dy-
841 namic weakening is an important topic for future work.

842 The models presented in this work consider changes in the pore fluid pressure due
843 to the thermal expansion of pore fluids and off-fault diffusion of heat and fluids, but do
844 not account for additional pore-scale fluid effects such as poroelastic stress changes or
845 dilatancy. Such effects should not substantially alter the conclusions of this work pro-
846 vided that the enhanced dynamic weakening - either due to thermal pressurization of
847 pore fluids as considered in this work, or due to other mechanisms - survives their ad-
848 dition. Dilatancy of the pore space during the initiation of unstable slip can stabilize slip
849 by decreasing the pore fluid pressure, and hence increasing shear resistance. However,
850 thermal pressurization is expected to overwhelm dilatancy at seismic slip rates during
851 dynamic rupture (e.g Segall et al., 2010), so the dilatancy should not substantially al-

852 ter the results for our models, unless the dilatancy is much greater than accounted for
853 by the commonly used formulation for dilatancy (Marone et al., 1990; Segall & Rice, 1995).
854 The effect of poroelasticity on rupture propagation is less known; however, it can cre-
855 ate an effective bimaterial response promoting slip in certain directions and discourag-
856 ing it in others (Dunham & Rice, 2008; Heimisson et al., 2019). The poroelastic effect
857 in studies so far is smaller than that of moderate or efficient thermal pressurization; for
858 example, the poroelastic changes in normal stress are 10% of friction change or less in
859 Dunham and Rice (2008). Both dilatancy and poroelastic effects warrant further study
860 in future work, including laboratory studies of dilatancy in well-slipped gouge layers typ-
861 ical of mature natural faults.

862 9 Conclusions

863 Our modeling of faults with rate-and-state friction and enhanced dynamic weak-
864 ening indicates that average shear prestress before dynamic rupture - which can serve
865 as a measure of average fault strength - can be scale-dependent and decrease with the
866 increasing rupture size. Such decrease is more prominent for faults with more efficient
867 dynamic weakening. The finding holds for faults with the standard rate-and-state fric-
868 tion only, without any additional dynamic weakening, although the dependence is rel-
869 atively unremarkable in that case (Figures 7 and S4). However, the scale-dependent de-
870 crease in average prestress is quite pronounced even for fault models with mild to mod-
871 erate enhanced dynamic weakening that satisfy a number of other field inferences, in-
872 cluding nearly magnitude-invariant static stress drops of 1-10 MPa, increasing average
873 breakdown energy with rupture size, radiation ratios between 0.1 and 1.0, and low-heat
874 fault operation (Perry et al., 2020; Lambert et al., 2021).

875 Our simulations illustrate that both critical fault stress required for rupture prop-
876 agation and static stress drops are products of complex finite-fault interactions, includ-
877 ing wave-mediated stress concentrations at the rupture front and redistribution of stress

878 post-rupture by dynamic waves. Hence it is important to keep in mind the finite-fault
879 effects - and their consequences in terms of the spatially variable fault prestress, slip rate,
880 and shear stress evolution - when interpreting single-degree-of-freedom representations,
881 such as spring-slider models and small-scale laboratory measurements. This consider-
882 ation highlights the need to continue developing a better physical understanding of fault-
883 ing at various scales through a combination and interaction of small-scale and intermediate-
884 scale lab and field experiments, constitutive relations formulated based on such exper-
885 iments, and finite-fault numerical modeling constrained by inferences from large-scale
886 field observations. Our comparison of local fault behavior in SDOF and dynamic rup-
887 ture simulations also demonstrate how small-scale experiments can be used in conjunc-
888 tion with finite-fault modeling to improve our understanding of the earthquake source:
889 the finite-fault modeling can suggest the initial conditions and slip-rate histories for the
890 small-scale experiments to impose, and then the shear stress evolution from the small-
891 scale experiments can be compared to the numerically obtained ones, which would al-
892 low to further improve the constitutive laws used in finite-fault modeling.

893 We find that increasingly efficient dynamic weakening leads to different earthquake
894 statistics, with fewer small events and increasingly more large events. This finding adds
895 to the body of work suggesting that enhanced dynamic weakening may be responsible
896 for deviations - inferred for large, mature fault segments - of earthquake statistics from
897 the Gutenberg-Richter scaling (Sieh, 1978; Bouchon & Karabulut, 2008; Hauksson et al.,
898 2012; Jiang & Lapusta, 2016; Michailos et al., 2019). For example, fault models with ef-
899 ficient dynamic weakening are consistent with mature faults that have historically hosted
900 large earthquakes but otherwise appear seismically quiescent, such as the Cholame and
901 Carrizo segments of the San Andreas Fault, which hosted the 1857 Fort Tejon earthquake
902 (Jiang & Lapusta, 2016). In contrast, the presence of a wider range of rupture sizes and
903 styles of slip transients on other faults, such as the Japan trench (e.g. Ito et al., 2013),
904 may suggest that they undergo more mild to moderate enhanced weakening during dy-
905 namic ruptures, and/or exhibit more pronounced fault heterogeneity.

Such considerations may be useful for earthquake early warning systems, which currently do not take into account the potential physics-based differences in the event-size distribution. Under the assumption of Gutenberg-Richter statistics, the probability that a smaller, Mw 5 or 6 event becomes a much larger earthquake is not great; however, that probability may be substantially larger on mature faults if they are indeed governed by enhanced dynamic weakening.

Our results indicate that critical stress conditions for earthquake occurrence cannot be described by a single number but rather present a complex spatial distribution with scale-dependent averages. When considering the critical stress conditions, it is essential to take into account both the size of the rupture and the weakening behavior, and hence the style of motion, that may occur throughout rupture propagation. These results warrant further investigation, specifically how the weakening behavior during dynamic rupture would interact with different degrees of fault heterogeneity as well as implications for earthquake early warning.

Parameter	Symbol	Value
Loading slip rate	V_{pl}	10^{-9} m/s
Shear wave speed	c_s	3299 m/s
Shear modulus	μ	36 GPa
Thermal diffusivity	α_{th}	10^{-6} m ² /s
Specific heat	ρ_c	2.7 MPa/K
Shear zone half-width	w	10 mm
Rate-and-state parameters		
Reference slip velocity	V_*	10^{-6} m/s
Reference friction coefficient	f_*	0.6
Rate-and-state direct effect (VW)	a	0.010
Rate-and-state evolution effect (VW)	b	0.015
Rate-and-state evolution effect (VS)	b	0.003
Length scales		
Fault length	λ	96 km
Frictional domain	λ_{fr}	72 km
Velocity-weakening region	λ_{VW}	24 km
Cell size	Δz	3.3 m
Quasi-static cohesive zone	Λ_0	84 m
Nucleation size (Rice & Ruina, 1983)	h_{RR}^*	226 m
Nucleation size (Rubin & Ampuero, 2005)	h_{RA}^*	550 m

Table 1. Model parameters used in all simulations unless otherwise specified.

Parameter	Symbol	TP 1	TP 2	TP 3	TP 4
Interseismic effective normal stress (MPa)	$\bar{\sigma} = (\sigma - p_{int})$	25	25	25	50
Rate-and-state direct effect (VS)	a	0.050	0.050	0.025	0.050
Characteristic slip (mm)	D_{RS}	1	1	1	2
Coupling coefficient (MPa/K)	Λ	0.1	0.34	0.34	0.34
Hydraulic diffusivity m ² /s	α_{hy}	10^{-3}	10^{-3}	10^{-4}	10^{-3}

Table 2. Parameters for models including thermal pressurization of pore fluids.

Parameter	Symbol	RS 1	RS 2
Interseismic effective normal stress (MPa)	$\bar{\sigma} = (\sigma - p_{int})$	10	20
Rate-and-state direct effect (VS)	a	0.050	0.050
Characteristic slip (mm)	D_{RS}	0.05	0.1
Quasi-static cohesive zone (m)	Λ_0	106	106
Nucleation size (m), Rice & Ruina, 1983	h_{RR}^*	282	282
Nucleation size (m), Rubin & Ampuero, 2005	h_{RA}^*	688	688

Table 3. Parameters for models including only standard rate-and-state friction.

Fault model	Slope c_1	Intercept c_2	STD ($\tau_{\text{ini}}^A / \tau_{\text{ss}}^{V_{\text{pl}}}$)
R1	6.51×10^{-2}	1.01	3.21×10^{-3}
R2	7.53×10^{-2}	1.01	2.39×10^{-3}
TP1	8.91×10^{-2}	1.00	4.40×10^{-3}
TP2	22.0×10^{-2}	1.01	7.68×10^{-3}
TP3	36.5×10^{-2}	1.04	3.74×10^{-3}
TP4	28.4×10^{-2}	0.930	10.9×10^{-3}

Table 4. Parameters from linear fit to trends in the ratio of the spatially averaged prestress τ_{ini}^A to SSQS shear resistance $\tau_{\text{ss}}^{V_{\text{pl}}}$ and log-10 of the ratio between rupture length λ_{rupt} and the theoretical nucleation length h_{RA}^* (equation 7, Figure 7C).

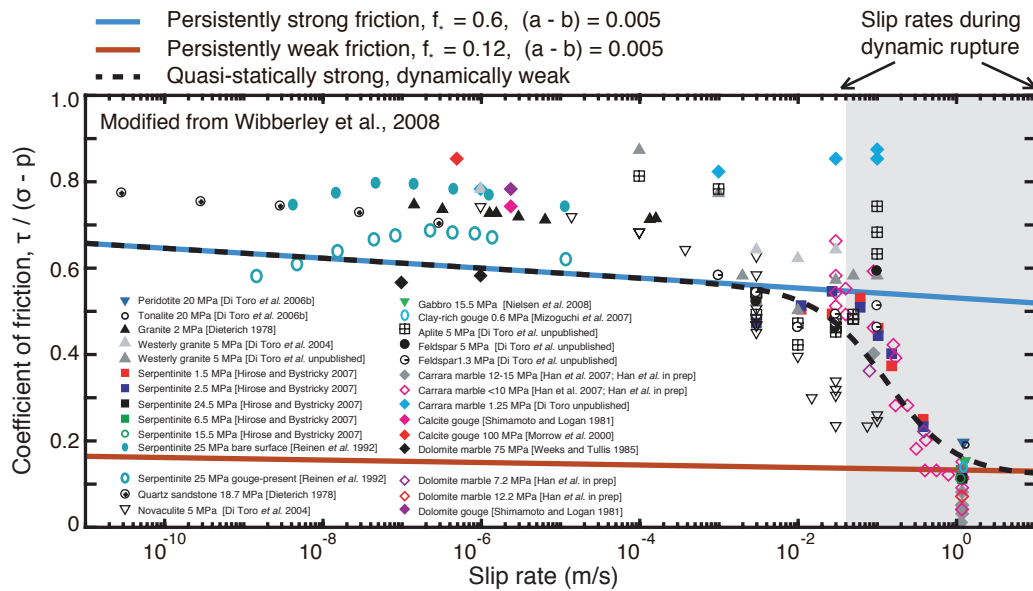


Figure 1. Field observations suggest that the average effective friction on mature faults must be low (< 0.1). One explanation for this inferred low effective friction would be that mature faults are persistently weak, such as from the presence of fault materials with persistently low friction coefficients $\tau / (\sigma - p)$ (red). Faults may also be persistently weak while having actual friction coefficients that are persistently high (> 0.2, blue), but require substantial chronic fluid overpressure in order to maintain low effective fault friction. A number of laboratory experiments indicate that the coefficient of friction for many materials relevant to seismogenic faults is around 0.6–0.8 at low sliding rates, but drops dramatically to lower values (< 0.2) at higher slip rates relevant to seismic slip, consistent with the notion of quasi-statically strong, but dynamically weak behavior (dashed black line).

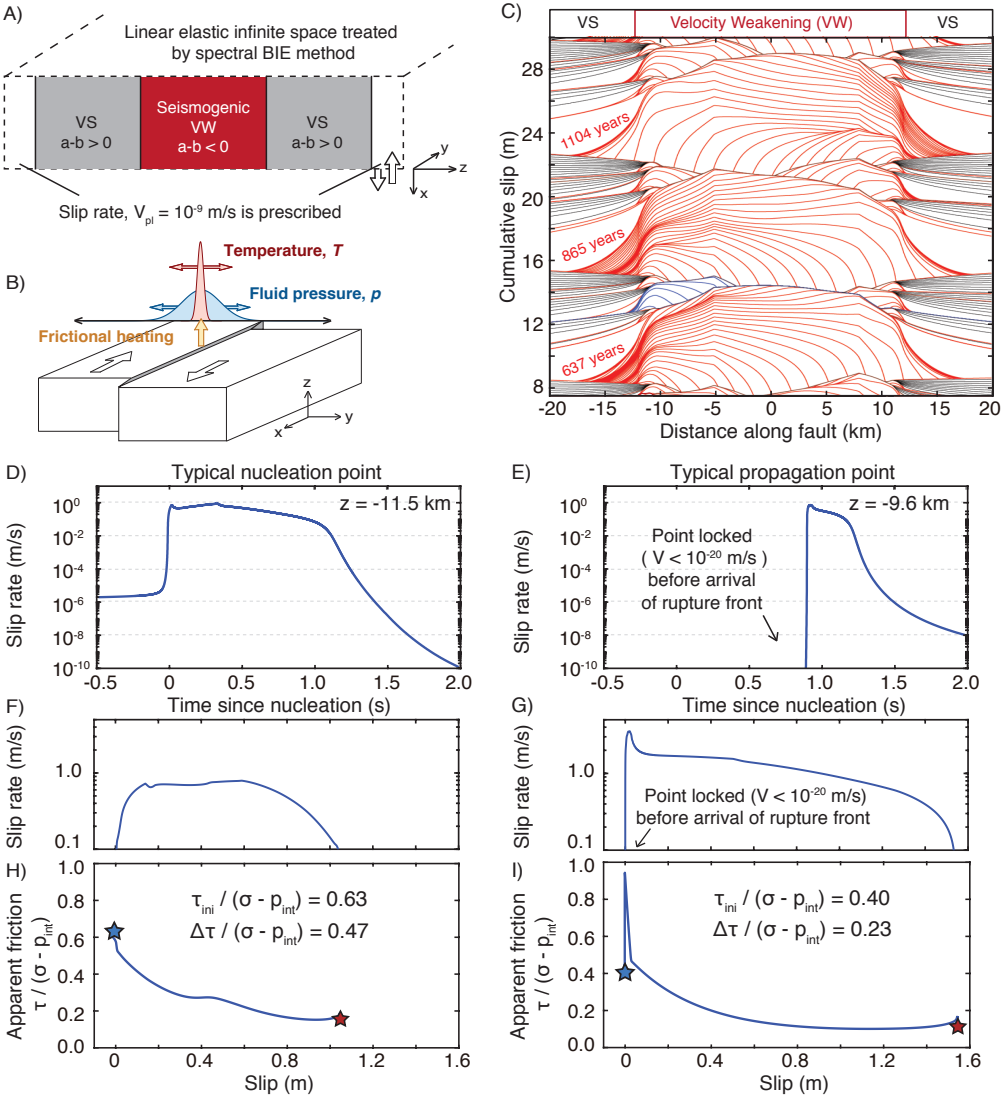


Figure 2. Modeling of sequences of earthquakes and aseismic slip on a rate-and-state fault with (A) a velocity-weakening (VW) seismogenic region surrounded by two velocity-strengthening (VS) sections and (B) enhanced dynamic weakening due to the thermal pressurization of pore fluids. The evolution of temperature and pore fluid pressure due to shear heating and off-fault diffusion is computed throughout our simulations. (C) A short section of the accumulated slip history in fault model TP3 (Table 2). Seismic events are illustrated by red lines plotted every 0.5 s while aseismic slip is shown by black lines plotted every 10 years. (D-G) Evolution of local slip rate with time and slip at points representative of nucleation and typical rupture propagation behavior within a crack-like rupture (colored blue in C). Points throughout rupture propagation (E & G) are initially locked and are driven to rupture by the concentration of dynamic stresses at the rupture front, thus experiencing more rapid acceleration of slip compared to points within the nucleation region (D & F). (H-I) The difference in local slip rate history contributes to a difference in the evolution of shear stress with slip. (H) Evolution of the apparent coefficient of friction $\tau / (\sigma - p_{int})$ with slip in the nucleation region is consistent with the laboratory notion of quasi-statically strong, dynamically weak behavior, with the apparent friction coefficient initially close to the reference value of 0.6 and dropping to a low dynamic resistance below 0.2 with slip. (I) Evolution of the apparent friction coefficient at points throughout rupture propagation is more complicated as the scaled prestress can be much lower than the reference friction before the arrival of the dynamic stress concentration.

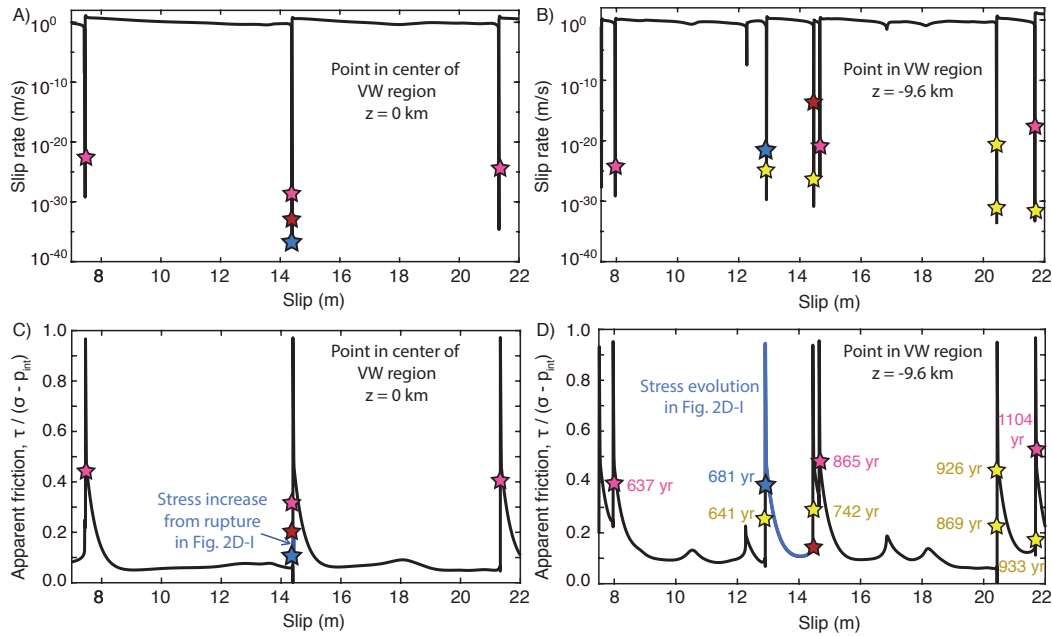


Figure 3. Evolution of the local slip rate and apparent friction coefficient at points within the velocity-weakening (VW) region with accumulating slip in fault model TP3 (Table 2). The stars denote instances in the earthquake sequence in Figure 2C, with pink stars marking the initiation of the three large model-spanning ruptures, the blue and red stars denoting the beginning and end of the moderate-sized rupture illustrated by blue contours, respectively. The yellow stars denote small to moderate-sized ruptures occurring along the VW-VS boundary at $z = -12 \text{ km}$. (A & C) The point in the center of the VW region ($z = 0 \text{ km}$) ruptures and experiences substantial slip only in large ruptures. The point exhibits an increase in shear stress over time due to the stress transfer from smaller ruptures that do not penetrate into the center of the VW region (such as the rupture colored blue in Fig. 2C). (B & D) Points closer to the boundary between the VW and VS regions can rupture during both smaller and large ruptures depending on the pre-stress conditions when ruptures arrive, resulting in a more complicated evolution of shear stress with accumulating slip. For both points in the VW region, the shear stress is brought to the peak stress and failure during ruptures by the dynamic stresses at the rupture front.

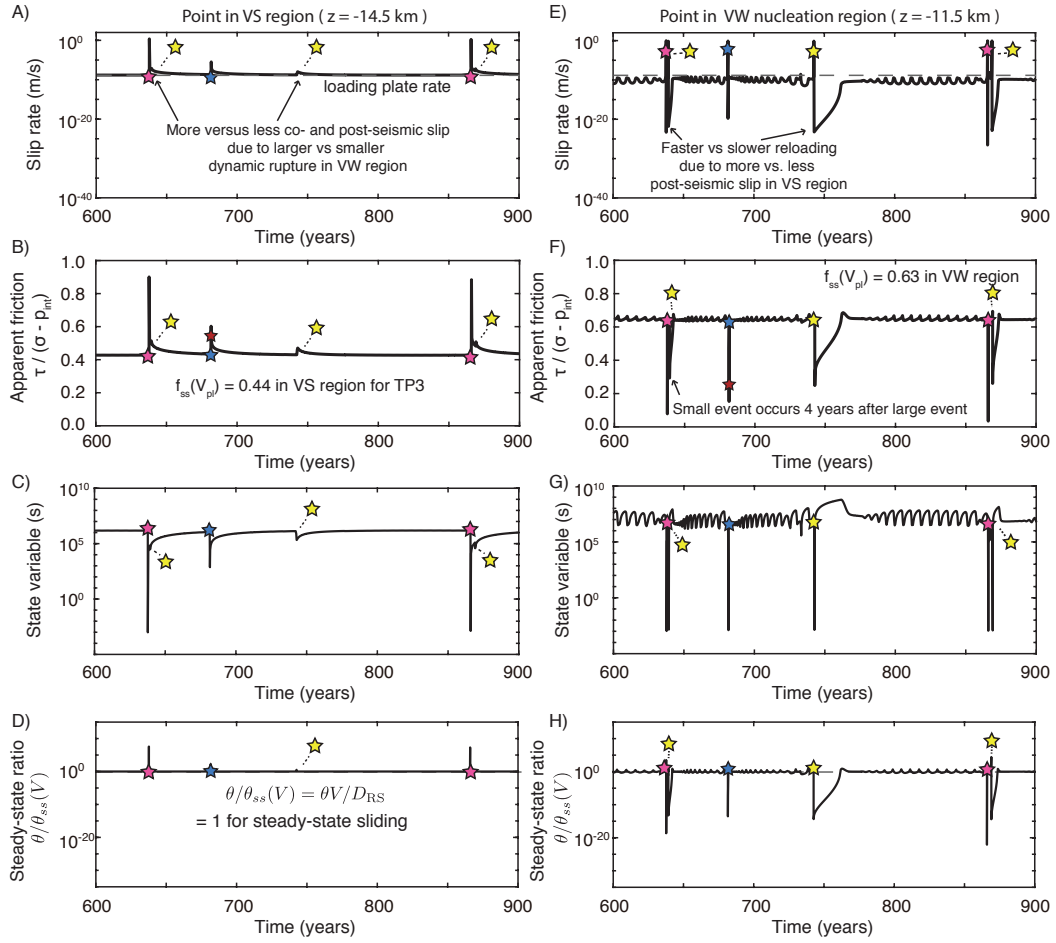


Figure 4. Evolution of local slip rate, apparent friction, and state variable at points near rupture nucleation between two model-spanning ruptures. The stars denote instances in the earthquake sequence in Figure 2C, with pink stars marking the initiation of the first two large model-spanning ruptures, the blue star denoting the beginning of the moderate-sized rupture illustrated by blue contours and the yellow stars denoting smaller ruptures. (A) Points within the VS region typically slip near the loading plate rate but can experience transient accelerated slip during and following ruptures occurring within the VW region. (B-D) The apparent friction coefficient and state variable in the VS region is typically near steady state, except during accelerated slip. (E-F) Slow slip penetrates into the VW region, driving points near the VW-VS boundary close to the loading slip rate, with the apparent friction coefficient being close to the corresponding steady-state value $f_{ss}(V_{pl})$. The slip rate and apparent friction exhibit small oscillations as the points near the VW-VS boundary continue to be loaded by slow slip in the VS region, accelerate, and weaken, thus transmitting stress further into the VW region until a sufficiently large region is loaded to sustain rupture nucleation and acceleration to seismic slip rates. The loading rate of the VW region also depends on the amount of accelerated slip in the VS due to previous ruptures (e.g. A & E around 650 vs. 750 years). (G-H) Following dynamic rupture, the state variable heals close to the steady-state value around the prescribed loading rate $\theta_{ss}(V_{pl})$ but continues to oscillate along with the unsteady slip resulting from the penetration of creep into the VW region, as seen in (E).

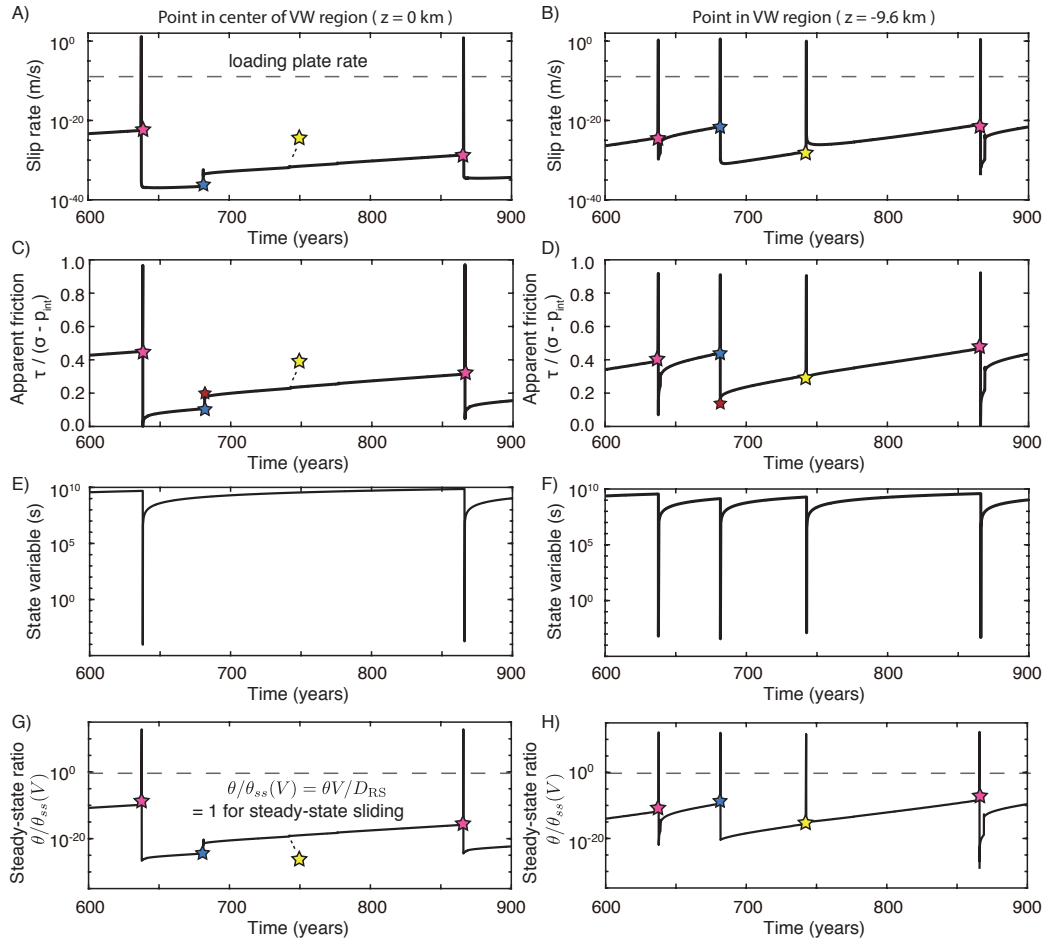


Figure 5. Evolution of local slip rate, apparent friction, and state variable at points within the VW region between two model-spanning ruptures. The stars denote instances in the earthquake sequence in Figure 2C, with pink stars marking the initiation of the first two large model-spanning ruptures, the blue star denoting the beginning of the moderate-sized rupture illustrated by blue contours and the yellow stars denoting smaller ruptures. (A-B) Points within the VW region are typically locked in between earthquake ruptures, sliding at slip rates far below the loading plate rate. (C-D) Loading from the VS regions as well as slip in neighboring ruptures leads to a time-dependent increase in shear stress. However, the points are still near-locked when dynamic rupture arrives from elsewhere, bringing a significant stress concentration and weakening on the timescale of the event which here collapses onto a vertical line. (E-F) The evolution of the state variable shows increase in the interseismic periods which encapsulate the fault healing and decrease to low values during earthquake rupture. (G-H) The ratio of the current value of the state variable θ to the steady-state value $\theta_{ss}(V)$, corresponding to the current local slip rate V , is much smaller than 1 during the interseismic periods, indicating the continued healing of shear resistance prior to rupture. As the slip rate rapidly accelerates during dynamic rupture, the state variable temporarily exceeds the new much lower steady-state values corresponding to the dynamic slip rate $\theta_{ss}(V_{dyn})$, then evolves to this lower steady-state value, and then falls to values below steady-state during the interseismic periods, indicating fault healing.

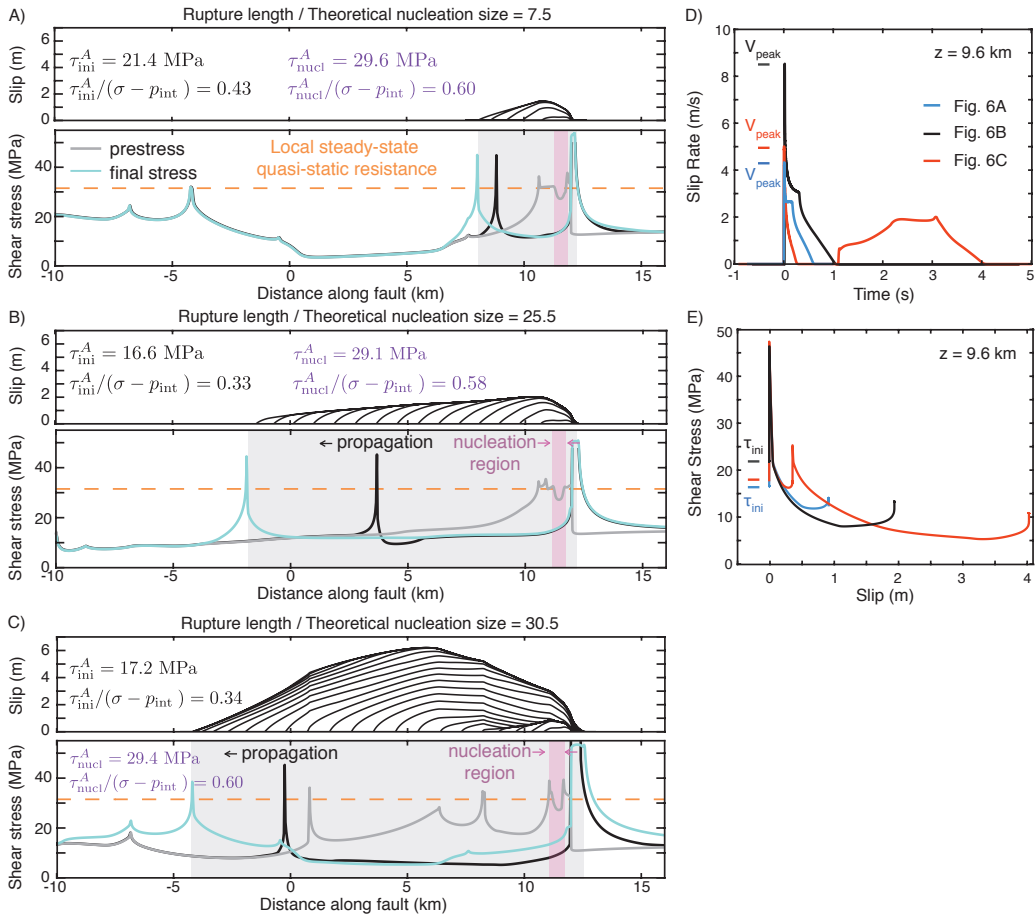


Figure 6. Spatial distribution of slip (top) and prestress and final shear stress (bottom) during three ruptures (A-C) with different rupture lengths in the same fault model (TP4 from Table 2). Slip contours are plotted every 0.25 s. The purple and gray shading illustrates the extent of the nucleation and ruptured regions, respectively, over which the prestress is averaged. While the ruptures nucleate in regions with stress levels near the local steady-state quasi-static shear resistance (dashed orange line), larger ruptures propagate over lower prestressed areas, resulting in lower average prestress and lower average coefficients of friction $\tau_{\text{ini}}^A/[\sigma - p_{\text{int}}]$. The shear stress distribution for a typical moment during rupture propagation is shown in black, demonstrating the stress concentration at the rupture front that brings the fault stress to values comparable to the SSQS shear resistance. The peak stress is even higher since the fault is initially dynamically stronger due to the rate-and-state direct effect. (D-E) Significant differences in local evolution of slip and stress at the same fault location ($z = 9.6 \text{ km}$) for different ruptures that depend on the prestress conditions due to previous slip events and the dynamic stress interactions during the individual ruptures.

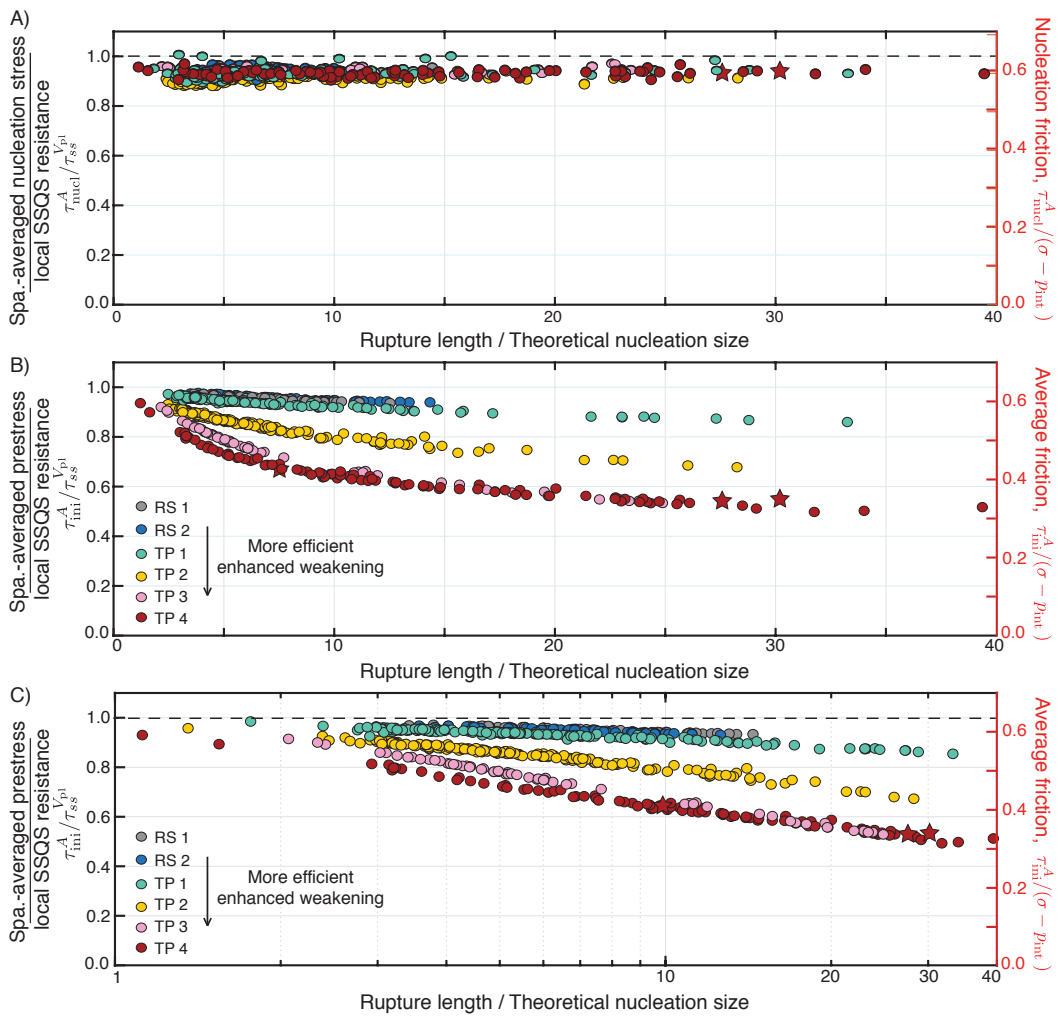


Figure 7. The difference between average shear stress needed for rupture nucleation vs. dynamic propagation. (A) The spatially-averaged nucleation stress τ_{nuc}^A for ruptures is comparable to the average local steady-state quasi-static shear resistance $\tau_{ss}^{V_{pl}}$, regardless of the final rupture size. (B-C) The spatially-averaged prestress τ_{ini}^A and average friction coefficient $\tau_{\text{ini}}^A / (\sigma - p_{\text{int}})$ decrease with increasing rupture size; the effect is more pronounced with increasing efficiency of weakening. The three ruptures shown in Figure 6 are denoted by red stars. (C) The decrease in average prestress with rupture size for our simulated ruptures is generally consistent with a power-law relationship with the ratio of the rupture length and nucleation size (equation 7, Table 4).

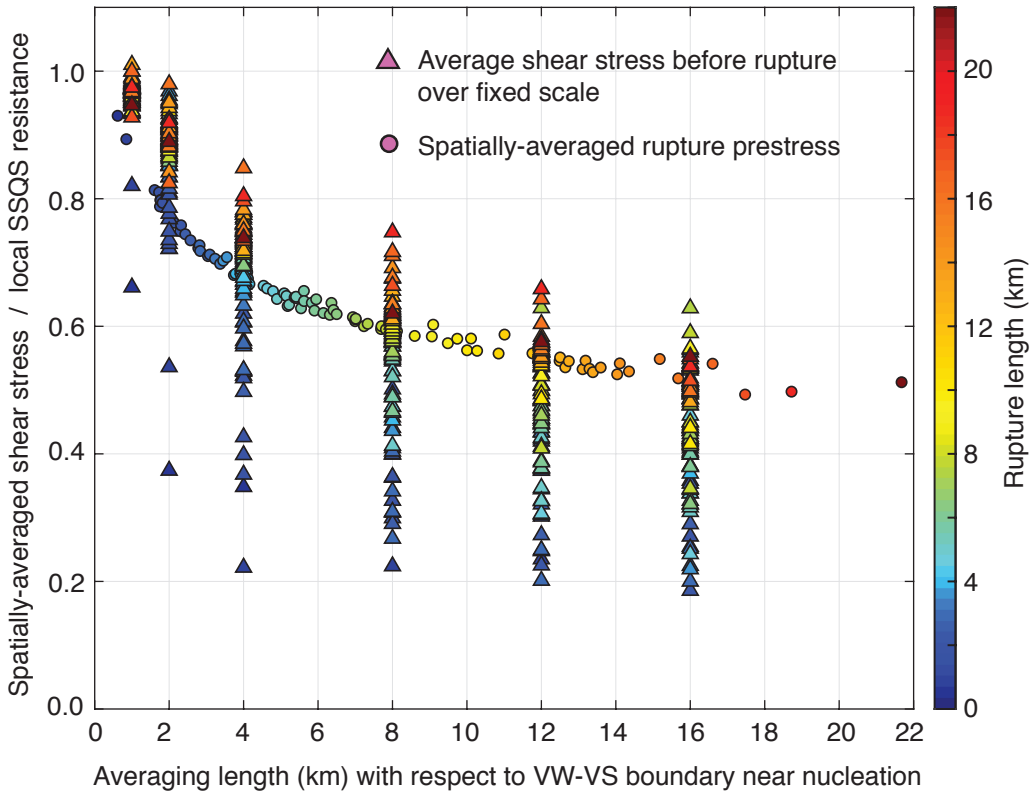


Figure 8. Comparison of the spatially averaged prestress over several fixed scales (1, 2, 4, 8, 12, and 16 km) and the average prestress over ruptures of varying size. As shown in Figure 7, the spatially-averaged prestress over the total rupture area τ_{ini}^A (circles) decreases considerably with rupture size in fault model TP4 from Table 2 with moderate enhanced dynamic weakening. However, larger ruptures have generally higher average shear stresses over smaller fixed scales around the nucleation region compared to smaller ruptures (red vs. blue triangles). The spatially-averaged shear stress over 1 km from the VW-VS boundary near the nucleation region of ruptures (triangles on the far-left) is relatively high (comparable to the local SSQS resistance) for both small and large ruptures, indicating that ruptures nucleate in regions of relatively high prestress compared to the average prestress over the entire rupture area (circles). For smaller ruptures, the average prestress at the fixed scales just larger than their total rupture length is lower than the average prestress of ruptures with comparable length to the fixed scale, suggesting that the prestress levels were too low to sustain further rupture propagation.

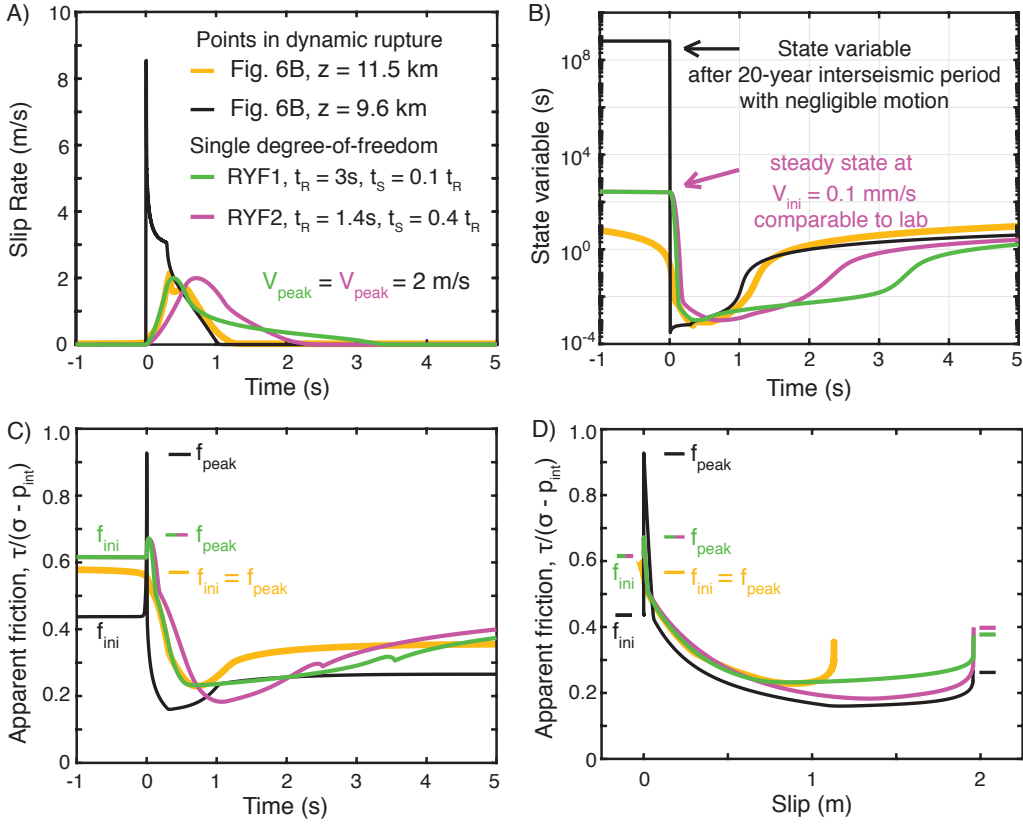


Figure 9. Comparison of the results of our dynamic modeling with a single-degree of freedom (SDOF) model that might more closely represent what would be obtained in laboratory experiments given the same constitutive properties and typical lab procedures. (A) Comparison of the local slip rate during nucleation ($z = 11.5 \text{ km}$, yellow) and typical propagation ($z = 9.6 \text{ km}$, black) of the simulated dynamic rupture of Figure 6B with the slip rate evolution that could be imposed in lab experiments represented by two regularized Yoffe functions (Tinti et al., 2005) with peak slip rate of 2 m/s and comparable slip to the point at $z = 9.6 \text{ km}$. The imposed regularized Yoffe functions are generally comparable to the evolution of slip within the nucleation region ($z = 11.5 \text{ km}$), however they do not capture the rapid acceleration of slip associated with the arrival of the rupture front at points of typical propagation, as observed at $z = 9.6 \text{ km}$. (B) Comparison of the state variable evolution from our finite-fault dynamic simulation and the SDOF simulation of the lab experiment. The simulated lab experiment starts with the steady-state conditions for 0.1 mm/s based on the experiments of Fukuyama and Mizoguchi (2010), which results in a much lower initial state value compared to the point $z = 9.6 \text{ km}$ in our simulations which, prior to dynamic rupture, had negligible motion over a 20-year interseismic period. (C-D) Evolution of the local apparent coefficient of friction with time and slip for the point in our simulated finite-fault dynamic rupture and simulated SDOF lab experiments. The dynamic weakening is generally comparable between the points in the finite rupture and the simulated SDOF experiments, however the evolution of shear stress substantially differ with regards to the much lower prestress at $z = 9.6 \text{ km}$ before the finite dynamic rupture and the abrupt increase and then decrease in stress due to the arrival of the dynamic rupture front and the associated rapid weakening.

Accepted Article

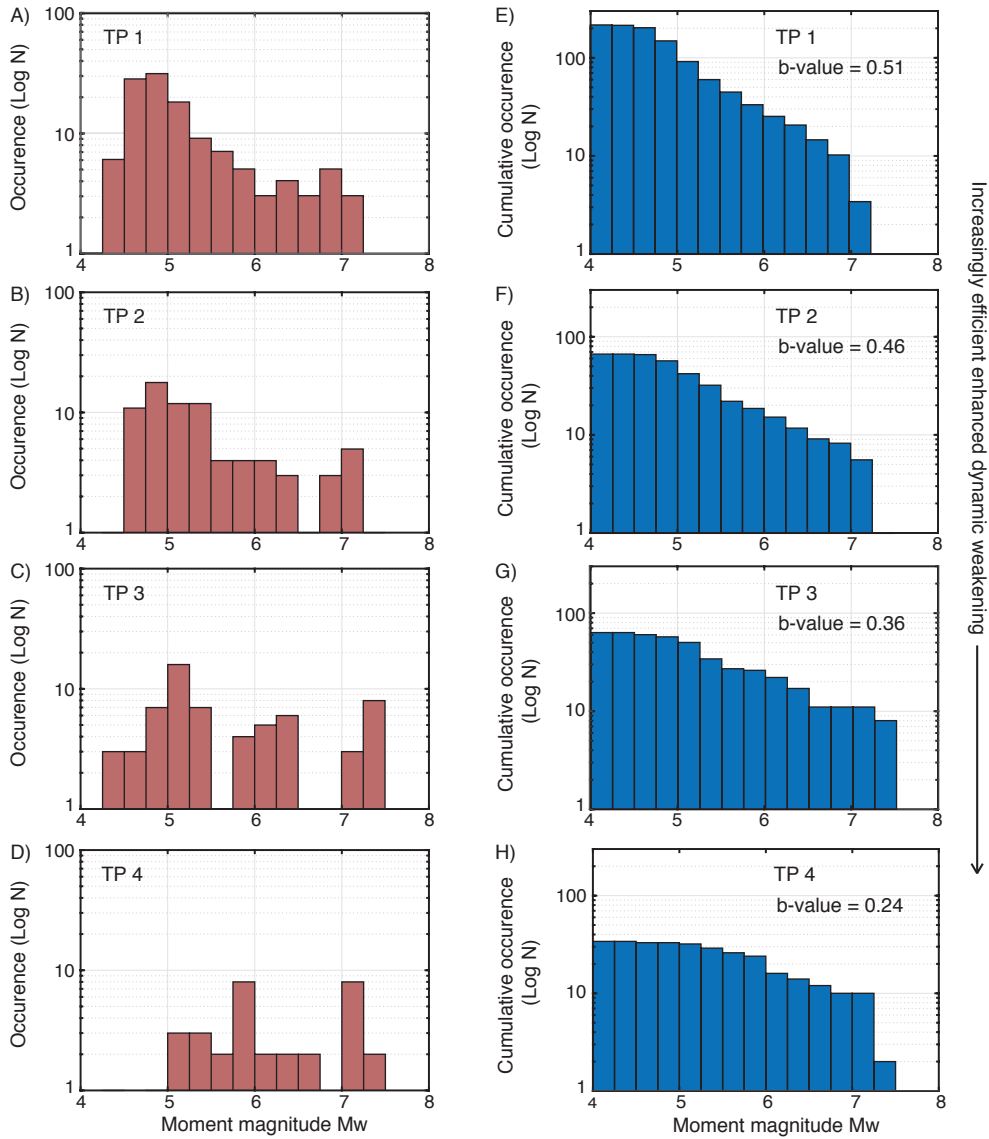


Figure 10. Fault models with more efficient weakening result in less earthquake sequence complexity, producing fewer smaller events (left column) and smaller b-values (right column). (A-D) Frequency-magnitude and (E-H) cumulative frequency-magnitude statistics for simulations with increasing efficiency of enhanced dynamic weakening (TP1-4 from Table 2).

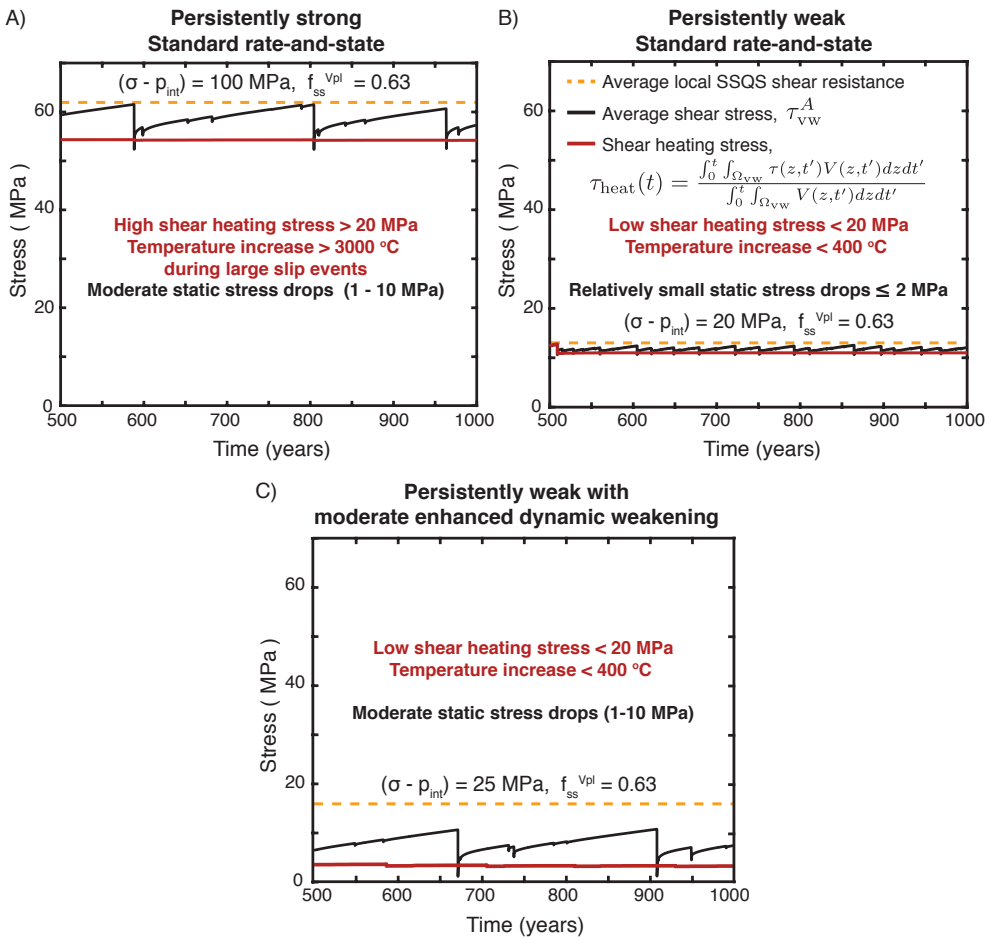


Figure 11. Evolution of the spatially averaged shear stress in the VW region τ_{vw}^A (black line) over earthquakes sequences. (A-B) Standard rate-and-state friction results in modest changes in shear resistance from the average local steady-state quasi-static (SSQS) shear resistance (orange line). Ruptures on persistently strong faults produce realistic static stress drops (A); however, the fault temperature would increase by more than 3000 °C during a dynamic event for a shear-zone half-width of 10 mm. (B) Persistently weak fault models due to low effective normal stress but with no enhanced weakening (RS 2 of Table 2) can maintain modest fault temperatures, but produce relatively small static stress drops $\leq 2 \text{ MPa}$. (C) Persistently weak models with mild to moderate enhanced dynamic weakening (TP3 of Table 2) are capable of maintaining modest fault temperatures and producing more moderate average stress drops between 1 - 10 MPa.

Acknowledgments

This study was supported by the National Science Foundation (grants EAR 1724686) and the Southern California Earthquake Center (SCEC), contribution No. 10782. SCEC is funded by NSF Cooperative Agreement EAR-1033462 and USGS Cooperative Agreement G12AC20038. D. Faulkner was supported by the Natural Environment Research Council (grants NE/P002943/1 and NE/R017484/1). The numerical simulations for this work were done on the High Performance Computing Central cluster of the California Institute of Technology. The data supporting the analysis and conclusions is given in Figures and Tables, in the main text and supplementary materials. Data is accessible through the CaltechDATA repository (<https://data.caltech.edu/records/1612>). We thank Tom Heaton, Hiroo Kanamori, Emily Brodsky, Mark Simons, Jean-Philippe Avouac and Zhongwen Zhan for helpful discussions and the Associate Editor and two anonymous reviewers for thoughtful suggestions that helped improve the manuscript.

References

- Acosta, M., Passelègue, F. X., Schubnel, A., & Violay, M. (2018). Dynamic weakening during earthquakes controlled by fluid thermodynamics. *Nature Communications*, 9(1), 3074. doi: 10.1038/s41467-018-05603-9
- Ader, T. J., Lapusta, N., Avouac, J.-P., & Ampuero, J.-P. (2014). Response of rate-and-state seismogenic faults to harmonic shear-stress perturbations. *Geophysical Journal International*, 198(1), 385-413. doi: 10.1093/gji/ggu144
- Allmann, B. P., & Shearer, P. M. (2009). Global variations of stress drop for moderate to large earthquakes. *Journal of Geophysical Research: Solid Earth*, 114(B1). doi: 10.1029/2008JB005821
- Ampuero, J.-P., Ripperger, J., & Mai, P. M. (2006). Properties of dynamic earthquake ruptures with heterogeneous stress drop. In *Earthquakes: Radiated energy and the physics of faulting* (p. 255-261). American Geophysical Union (AGU). doi: <https://doi.org/10.1029/170GM25>

- 947 Andrews, D. J. (2004, 06). Rupture Models with Dynamically Determined Break-
 948 down Displacement. *Bulletin of the Seismological Society of America*, 94(3),
 949 769-775. doi: 10.1785/0120030142
- 950 Bandis, S., Lumsden, A., & Barton, N. (1981). Experimental studies of scale effects
 951 on the shear behaviour of rock joints. *International Journal of Rock Mechanics
 and Mining Sciences & Geomechanics Abstracts*, 18(1), 1 - 21. doi: [https://doi.org/10.1016/0148-9062\(81\)90262-X](https://doi.org/10.1016/0148-9062(81)90262-X)
- 952
- 953 Bangs, N., Moore, G., Gulick, S., Pangborn, E., Tobin, H., Kuramoto, S., & Taira,
 954 A. (2009). Broad, weak regions of the Nankai Megathrust and implications for
 955 shallow coseismic slip. *Earth and Planetary Science Letters*, 284(1), 44 - 49.
- 956 Barbot, S. (2019). Slow-slip, slow earthquakes, period-two cycles, full and partial
 957 ruptures, and deterministic chaos in a single asperity fault. *Tectonophysics*,
 958 768, 228171. doi: <https://doi.org/10.1016/j.tecto.2019.228171>
- 959
- 960 Beeler, N., Kilgore, B., McGarr, A., Fletcher, J., Evans, J., & Baker, S. R. (2012).
 961 Observed source parameters for dynamic rupture with non-uniform ini-
 962 tial stress and relatively high fracture energy. *Journal of Structural Ge-
 963 ology*, 38, 77-89. (Physico-Chemical Processes in Seismic Faults) doi:
 964 <https://doi.org/10.1016/j.jsg.2011.11.013>
- 965 Ben-David, O., Cohen, G., & Fineberg, J. (2010). The dynamics of the onset of fric-
 966 tional slip. *Science*, 330(6001), 211–214. doi: 10.1126/science.1194777
- 967 Bhattacharya, P., Rubin, A. M., Bayart, E., Savage, H. M., & Marone, C. (2015).
 968 Critical evaluation of state evolution laws in rate and state friction: Fitting
 969 large velocity steps in simulated fault gouge with time-, slip-, and stress-
 970 dependent constitutive laws. *Journal of Geophysical Research: Solid Earth*,
 971 120(9), 6365-6385. doi: 10.1002/2015JB012437
- 972 Bhattacharya, P., Rubin, A. M., & Beeler, N. M. (2017). Does fault strengthening
 973 in laboratory rock friction experiments really depend primarily upon time and
 974 not slip? *Journal of Geophysical Research: Solid Earth*, 122(8), 6389-6430.

- 975 doi: 10.1002/2017JB013936
- 976 Blanpied, M. L., Lockner, D. A., & Byerlee, J. D. (1991). Fault stability inferred
977 from granite sliding experiments at hydrothermal conditions. *Geophysical Re-*
978 *search Letters*, 18(4), 609-612. doi: 10.1029/91GL00469
- 979 Blanpied, M. L., Lockner, D. A., & Byerlee, J. D. (1995). Frictional slip of gran-
980 ite at hydrothermal conditions. *Journal of Geophysical Research: Solid Earth*,
981 100(B7), 13045-13064. doi: 10.1029/95JB00862
- 982 Bouchon, M., & Karabulut, H. (2008). The aftershock signature of supershear earth-
983 quakes. *Science*, 320(5881), 1323-1325. doi: 10.1126/science.1155030
- 984 Brodsky, E. E., Kirkpatrick, J. D., & Candela, T. (2016, 01). Constraints from fault
985 roughness on the scale-dependent strength of rocks. *Geology*, 44(1), 19-22. doi:
986 10.1130/G37206.1
- 987 Brown, K., Kopf, A., Underwood, M., & Weinberger, J. (2003). Compositional and
988 fluid pressure controls on the state of stress on the nankai subduction thrust:
989 A weak plate boundary. *Earth and Planetary Science Letters*, 214(3), 589 -
990 603.
- 991 Brune, J. N., Henyey, T. L., & Roy, R. F. (1969). Heat flow, stress, and rate of
992 slip along the San Andreas Fault, California. *Journal of Geophysical Research*,
993 74(15), 3821-3827.
- 994 Byerlee, J. (1978). Friction of rocks. *Pure and Applied Geophysics*, 116(4-5), 615-
995 626. doi: 10.1007/BF00876528
- 996 Cattania, C. (2019). Complex earthquake sequences on simple faults. *Geophysical
997 Research Letters*, 46(17-18), 10384-10393. doi: 10.1029/2019GL083628
- 998 Cattania, C., & Segall, P. (2021). Precursory slow slip and foreshocks on rough
999 faults. *Journal of Geophysical Research: Solid Earth*, 126(4), e2020JB020430.
1000 (e2020JB020430 2020JB020430) doi: <https://doi.org/10.1029/2020JB020430>
- 1001 Chen, J., Verberne, B. A., & Spiers, C. J. (2015a). Effects of healing on the seis-
1002 mogenic potential of carbonate fault rocks: Experiments on samples from the

- 1003 Longmenshan Fault, Sichuan, China. *Journal of Geophysical Research: Solid*
 1004 *Earth*, 120(8), 5479-5506. doi: <https://doi.org/10.1002/2015JB012051>
- 1005 Chen, J., Verberne, B. A., & Spiers, C. J. (2015b). Interseismic re-strengthening
 1006 and stabilization of carbonate faults by "non-Dieterich" healing under hy-
 1007 drothermal conditions. *Earth and Planetary Science Letters*, 423, 1 - 12. doi:
 1008 <https://doi.org/10.1016/j.epsl.2015.03.044>
- 1009 Chen, T., & Lapusta, N. (2009). Scaling of small repeating earthquakes explained by
 1010 interaction of seismic and aseismic slip in a rate and state fault model. *Journal*
 1011 *of Geophysical Research*, 114. doi: 10.1029/2008JB005749
- 1012 Chen, T., & Lapusta, N. (2019, 06). On behaviour and scaling of small repeating
 1013 earthquakes in rate and state fault models. *Geophysical Journal International*,
 1014 218(3), 2001-2018. doi: 10.1093/gji/ggz270
- 1015 Collettini, C., Niemeijer, A., Viti, C., & Marone, C. (2009). Fault zone fabric and
 1016 fault weakness. *Nature*, 462(7275), 907–910. doi: 10.1038/nature08585
- 1017 De Paola, N., Holdsworth, R. E., Viti, C., Collettini, C., & Bullock, R. (2015).
 1018 Can grain size sensitive flow lubricate faults during the initial stages of earth-
 1019 quake propagation? *Earth and Planetary Science Letters*, 431, 48 - 58. doi:
 1020 <https://doi.org/10.1016/j.epsl.2015.09.002>
- 1021 Di Toro, G., Han, R., Hirose, T., De Paola, N., Nielsen, S., Mizoguchi, K., ... Shi-
 1022 mamoto, T. (2011). Fault lubrication during earthquakes. *Nature*, 471,
 1023 494.
- 1024 Dieterich, J. H. (1979). Modeling of rock friction 1. Experimental results and consti-
 1025 tutive equations. *Journal of Geophysical Research*, 84(B5), 2161-2168.
- 1026 Dieterich, J. H., & Kilgore, B. D. (1994). Direct observation of frictional contacts:
 1027 New insights for state-dependent properties. *Pure and Applied Geophysics*,
 1028 143, 283?302. doi: 10.1007/BF00874332
- 1029 Dunham, E. M., Belanger, D., Cong, L., & Kozdon, J. E. (2011). Earthquake
 1030 ruptures with strongly rate-weakening friction and off-fault plasticity, part

- 1031 1: Planar faults. *Bulletin of the Seismological Society of America*, 101(5),
 1032 2296-2307. doi: 10.1785/0120100075
- 1033 Dunham, E. M., & Rice, J. R. (2008). Earthquake slip between dissimilar poro-
 1034 elastic materials. *Journal of Geophysical Research: Solid Earth*, 113(B9). doi:
 1035 <https://doi.org/10.1029/2007JB005405>
- 1036 Erickson, B. A., Jiang, J., Barall, M., Lapusta, N., Dunham, E. M., Harris, R., ...
 1037 Wei, M. (2020). The community code verification exercise for simulating
 1038 sequences of earthquakes and aseismic slip (SEAS). *Seismological Research
 Letters*, 91(2A), 874–890. doi: 10.1785/0220190248
- 1039 Fang, Z., & Dunham, E. M. (2013). Additional shear resistance from fault rough-
 1040 ness and stress levels on geometrically complex faults. *Journal of Geophysical
 Research: Solid Earth*, 118(7), 3642-3654. doi: 10.1002/jgrb.50262
- 1041 Faulkner, D. R., Mitchell, T. M., Behnson, J., Hirose, T., & Shimamoto, T. (2011).
 1042 Stuck in the mud? Earthquake nucleation and propagation through accre-
 1043 tionary forearcs. *Geophysical Research Letters*, 38(18). doi: <https://doi.org/10.1029/2011GL048552>
- 1044 Faulkner, D. R., Mitchell, T. M., Healy, D., & Heap, M. J. (2006). Slip on 'weak'
 1045 faults by the rotation of regional stress in the fracture damage zone. *Nature*,
 1046 444(7121), 922–925. doi: 10.1038/nature05353
- 1047 Field, E. H., Biasi, G., Bird, P., Dawson, T., Felzer, K.R., ... Zeng, Y. (2013).
 1048 Uniform California Earthquake Rupture Forecast, version 3 (UCERF3):
 1049 The time-independent model. *U.S. Geological Survey Open-File Report
 2013-1165, 97 p.*, California Geological Survey Special Report 228. doi:
 1050 <http://pubs.usgs.gov/of/2013/1165/>
- 1051 Field, E. H., Jordan, T. H., Page, M. T., Milner, K. R., Shaw, B. E., Dawson, T. E.,
 1052 ... Thatcher, W. R. (2017). A synoptic view of the third Uniform California
 1053 Earthquake Rupture Forecast (UCERF3). *Seismological Research Letters*,
 1054 88(5), 1259-1267. doi: 10.1785/0220170045

- 1059 Fineberg, J., & Bouchbinder, E. (2015). Recent developments in dynamic fracture:
1060 Some perspectives. *International Journal of Fracture*, 196(1), 33–57. doi: 10
1061 .1007/s10704-015-0038-x
- 1062 Freund, L. B. (1990). *Dynamic fracture mechanics*. Cambridge University Press. doi:
1063 10.1017/CBO9780511546761
- 1064 Fukuyama, E., & Mizoguchi, K. (2010). Constitutive parameters for earthquake rup-
1065 ture dynamics based on high-velocity friction tests with variable sliprate. *In-*
1066 *ternational Journal of Fracture*, 163(1), 15–26. doi: 10.1007/s10704-009-9417
1067 -5
- 1068 Fulton, P. M., Brodsky, E. E., Kano, Y., Mori, J., Chester, F., Ishikawa, T., ...
1069 Scientists, K.-. (2013). Low coseismic friction on the Tohoku-Oki fault deter-
1070 mined from temperature measurements. *Science*, 342(6163), 1214–1217. doi:
1071 10.1126/science.1243641
- 1072 Gabriel, A.-A., Ampuero, J.-P., Dalguer, L. A., & Mai, P. M. (2012). The tran-
1073 sition of dynamic rupture styles in elastic media under velocity-weakening
1074 friction. *Journal of Geophysical Research: Solid Earth*, 117(B9). doi:
1075 10.1029/2012JB009468
- 1076 Galis, M., Ampuero, J. P., Mai, P. M., & Cappa, F. (2017). Induced seismicity pro-
1077 vides insight into why earthquake ruptures stop. *Science Advances*, 3(12). doi:
1078 10.1126/sciadv.aap7528
- 1079 Gao, X., & Wang, K. (2014). Strength of stick-slip and creeping subduction megath-
1080 ruts from heat flow observations. *Science*, 345(6200), 1038-1041. doi: 10
1081 .1126/science.1255487
- 1082 Goldsby, D. L., & Tullis, T. E. (2011). Flash heating leads to low frictional strength
1083 of crustal rocks at earthquake slip rates. *Science*, 334(6053), 216–218. doi: 10
1084 .1126/science.1207902
- 1085 Greer, J. R., Oliver, W. C., & Nix, W. D. (2005). Size dependence of mechanical
1086 properties of gold at the micron scale in the absence of strain gradients. *Acta*

- 1087 *Materialia*, 53(6), 1821 - 1830. doi: <https://doi.org/10.1016/j.actamat.2004.12.031>
- 1089 Gu, J.-C., Rice, J. R., Ruina, A. L., & Tse, S. T. (1984). Slip motion and stability
1090 of a single degree of freedom elastic system with rate and state dependent fric-
1091 tion. *Journal of the Mechanics and Physics of Solids*, 32(3), 167 - 196. doi:
1092 [https://doi.org/10.1016/0022-5096\(84\)90007-3](https://doi.org/10.1016/0022-5096(84)90007-3)
- 1093 Han, R., Shimamoto, T., Ando, J.-i., & Ree, J.-H. (2007). Seismic slip record in
1094 carbonate-bearing fault zones: An insight from high-velocity friction experi-
1095 ments on siderite gouge. *Geology*, 35(12), 1131-1134.
- 1096 Hardebeck, J. L. (2015). Stress orientations in subduction zones and the strength of
1097 subduction megathrust faults. *Science*, 349(6253), 1213–1216. doi: 10.1126/
1098 science.aac5625
- 1099 Hardebeck, J. L., & Hauksson, E. (1999). Role of fluids in faulting inferred from
1100 stress field signatures. *Science*, 285(5425), 236–239. doi: 10.1126/science.285
1101 .5425.236
- 1102 Hardebeck, J. L., & Hauksson, E. (2001). Crustal stress field in Southern Cali-
1103 fornia and its implications for fault mechanics. *Journal of Geophysical Re-*
1104 *search: Solid Earth*, 106(B10), 21859-21882. doi: <https://doi.org/10.1029/2001JB000292>
- 1106 Hauksson, E., Yang, W., & Shearer, P. M. (2012). Waveform relocated earthquake
1107 catalog for Southern California (1981 to June 2011). *Bulletin of the Seismolog-*
1108 *ical Society of America*, 102(5), 2239-2244. doi: 10.1785/0120120010
- 1109 Heaton, T. H. (1990). Evidence for and implications of self-healing pulses of slip
1110 in earthquake rupture. *Physics of the Earth and Planetary Interiors*, 64(1), 1-
1111 20.
- 1112 Heimisson, E. R. (2020). Crack to pulse transition and magnitude statistics dur-
1113 ing earthquake cycles on a self-similar rough fault. *Earth and Planetary Sci-*
1114 *ence Letters*, 537, 116202. doi: <https://doi.org/10.1016/j.epsl.2020.116202>

- Heimisson, E. R., Dunham, E. M., & Almquist, M. (2019). Poroelastic effects destabilize mildly rate-strengthening friction to generate stable slow slip pulses. *Journal of the Mechanics and Physics of Solids*, 130, 262-279. doi: <https://doi.org/10.1016/j.jmps.2019.06.007>
- Henyey, T. L., & Wasserburg, G. J. (1971). Heat flow near major strike-slip faults in California. *Journal of Geophysical Research (1896-1977)*, 76(32), 7924-7946. doi: 10.1029/JB076i032p07924
- Herrendörfer, R., van Dithner, Y., Gerya, T., & Dalguer, L. A. (2015). Earthquake supercycle in subduction zones controlled by the width of the seismogenic zone. *Nature Geoscience*, 8(6), 471-474. Retrieved from <https://doi.org/10.1038/ngeo2427> doi: 10.1038/ngeo2427
- Hillers, G., Ben-Zion, Y., & Mai, P. M. (2006). Seismicity on a fault controlled by rate- and state-dependent friction with spatial variations of the critical slip distance. *Journal of Geophysical Research*, 111, B01403. doi: 10.1029/2005JB003859
- Hillers, G., Mai, P. M., Ben-Zion, Y., & Ampuero, J.-P. (2007). Statistical properties of seismicity of fault zones at different evolutionary stages. *Geophysical Journal International*, 169(2), 515-533. doi: 10.1111/j.1365-246X.2006.03275.X
- Ikari, M. J., Marone, C., & Saffer, D. M. (2011). On the relation between fault strength and frictional stability. *Geology*, 39(1), 83-86. doi: 10.1130/G31416.1
- Ishibe, T., & Shimazaki, K. (2012). Characteristic earthquake model and seismicity around late quaternary archive faults in Japan. *Bulletin of the Seismological Society of America*, 102(3), 1041-1058. doi: 10.1785/0120100250
- Ito, Y., Hino, R., Kido, M., Fujimoto, H., Osada, Y., Inazu, D., ... Ashi, J. (2013). Episodic slow slip events in the Japan subduction zone before the 2011 Tohoku-Oki earthquake. *Tectonophysics*, 600, 14-26. doi:

- 1143 https://doi.org/10.1016/j.tecto.2012.08.022
- 1144 Jaeger, J., & Cook, N. (1976). *Fundamentals of rock mechanics*. London, UK: Chap-
- 1145 man and Hall.
- 1146 Jiang, J., & Lapusta, N. (2016). Deeper penetration of large earthquakes on seis-
- 1147 mically quiescent faults. *Science*, 352(6291), 1293–1297. doi: 10.1126/science
- 1148 .aaf1496
- 1149 Kagan, Y. Y., Jackson, D. D., & Geller, R. J. (2012). Characteristic earthquake
- 1150 model, 1884–2011, RIP. *Seismological Research Letters*, 83(6), 951-953. doi:
- 1151 10.1785/0220120107
- 1152 Kaneko, Y., & Lapusta, N. (2008). Variability of earthquake nucleation in con-
- 1153 tinuum models of rate-and-state faults and implications for aftershock rates.
- 1154 *Journal of Geophysical Research*, 113, B12312. doi: 10.1029/2007JB005154
- 1155 Kato, N., & Tullis, T. E. (2001). A composite rate- and state-dependent law for
- 1156 rock friction. *Geophysical Research Letters*, 28(6), 1103-1106. doi: 10.1029/
- 1157 2000GL012060
- 1158 Lachenbruch, A. H., & Sass, J. H. (1980). Heat flow and energetics of the San
- 1159 Andreas Fault zone. *Journal of Geophysical Research: Solid Earth*, 85(B11),
- 1160 6185-6222. doi: 10.1029/JB085iB11p06185
- 1161 Lambert, V., & Lapusta, N. (2020). Rupture-dependent breakdown energy in
- 1162 fault models with thermo-hydro-mechanical processes. *Solid Earth*, 11(6),
- 1163 2283-2302. doi: 10.5194/se-11-2283-2020
- 1164 Lambert, V., Lapusta, N., & Perry, S. (2021). Propagation of large earthquakes as
- 1165 self-healing pulses or mild cracks. *Nature*, 591(7849), 252–258. doi: 10.1038/
- 1166 s41586-021-03248-1
- 1167 Lapusta, N., & Rice, J. (2003). Low-heat and low-stress fault operation in earth-
- 1168 quake models of statically strong but dynamically weak faults. *AGU Fall Meet-*
- 1169 *ing Abstracts*.
- 1170 Lapusta, N., Rice, J. R., Ben-Zion, Y., & Zheng, G. (2000). Elastodynamic analysis

- for slow tectonic loading with spontaneous rupture episodes on faults with
rate- and state-dependent friction. *Journal of Geophysical Research*, 105,
765–789. doi: 10.1029/2000JB900250
- Lockner, D. A., Morrow, C., Moore, D., & Hickman, S. (2011). Low strength of deep
San Andreas fault gouge from SAFOD core. *Nature*, 472(7341), 82–85. doi: 10
.1038/nature09927
- Lu, X., Rosakis, A. J., & Lapusta, N. (2010). Rupture modes in laboratory earth-
quakes: Effect of fault prestress and nucleation conditions. *Journal of Geophys-
ical Research: Solid Earth*, 115(B12). doi: 10.1029/2009JB006833
- Marone, C. (1998). Laboratory-derived friction laws and their application to seismic
faulting. *Annual Review of Earth and Planetary Sciences*, 26(1), 643–696. doi:
10.1146/annurev.earth.26.1.643
- Marone, C., Raleigh, C. B., & Scholz, C. H. (1990). Frictional behavior and
constitutive modeling of simulated fault gouge. *Journal of Geophysical
Research: Solid Earth*, 95(B5), 7007–7025. doi: [https://doi.org/10.1029/
JB095iB05p07007](https://doi.org/10.1029/JB095iB05p07007)
- McLaskey, G. C., Kilgore, B. D., Lockner, D. A., & Beeler, N. M. (2014). Labora-
tory generated M-6 earthquakes. *Pure and Applied Geophysics*, 171(10), 2601–
2615. doi: 10.1007/s00024-013-0772-9
- Michailos, K., Smith, E. G., Chamberlain, C. J., Savage, M. K., & Townend, J.
(2019). Variations in seismogenic thickness along the Central Alpine Fault,
New Zealand, revealed by a decade's relocated microseismicity. *Geochemistry,
Geophysics, Geosystems*, 20(1), 470–486. doi: 10.1029/2018GC007743
- Michel, S., Avouac, J.-P., Lapusta, N., & Jiang, J. (2017). Pulse-like partial ruptures
and high-frequency radiation at creeping-locked transition during megath-
rust earthquakes. *Geophysical Research Letters*, 44(16), 8345–8351. doi:
10.1002/2017GL074725
- Nankali, H. R. (2011, April). Slip rate of the Kazerun Fault and Main Recent Fault

- 1199 (Zagros, Iran) from 3D mechanical modeling. *Journal of Asian Earth Sciences*,
 1200 41, 89-98. doi: 10.1016/j.jseaes.2010.12.009
- 1201 Nielsen, S., Spagnuolo, E., Violay, M., Smith, S., Di Toro, G., & Bistacchi, A.
 1202 (2016). G: Fracture energy, friction and dissipation in earthquakes. *Journal
 of Seismology*, 20(4), 1187–1205. doi: 10.1007/s10950-016-9560-1
- 1203 Noda, H., Dunham, E. M., & Rice, J. R. (2009). Earthquake ruptures with
 1204 thermal weakening and the operation of major faults at low overall stress
 1205 levels. *Journal of Geophysical Research: Solid Earth*, 114(B7). doi:
 1206 10.1029/2008JB006143
- 1207 Noda, H., & Lapusta, N. (2010). Three-dimensional earthquake sequence simulations
 1208 with evolving temperature and pore pressure due to shear heating: Effect of
 1209 heterogeneous hydraulic diffusivity. *Journal of Geophysical Research*, 115,
 1210 B123414. doi: 10.1029/2010JB007780
- 1211 Noda, H., & Lapusta, N. (2012). On averaging interface response during dynamic
 1212 rupture and energy partitioning diagrams for earthquakes. *Journal of Applied
 Mechanics*, 79. doi: 10.1115/1.4005964
- 1213 Noda, H., Lapusta, N., & Kanamori, H. (2013). Comparison of average stress
 1214 drop measures for ruptures with heterogeneous stress change and impli-
 1215 cations for earthquake physics. *Geophysical Journal International*. doi:
 1216 10.1093/gji/ggt074
- 1217 Page, M. T., & Felzer, K. (2015). Southern San Andreas Fault seismicity is
 1218 consistent with the Gutenberg-Richter magnitude-frequency distribution.
 1219 *Bulletin of the Seismological Society of America*, 105(4), 2070-2080. doi:
 1220 10.1785/0120140340
- 1221 Page, M. T., & van der Elst, N. J. (2018). Fault-tolerant b-values and aftershock
 1222 productivity. *Journal of Geophysical Research: Solid Earth*, 123(12), 10,880-
 1223 10,888. doi: <https://doi.org/10.1029/2018JB016445>
- 1224 Perrin, G., Rice, J. R., & Zheng, G. (1995). Self-healing slip pulse on a frictional

- 1227 surface. *Journal of the Mechanics and Physics of Solids*, *43*(9), 1461 - 1495.
 1228 doi: [https://doi.org/10.1016/0022-5096\(95\)00036-I](https://doi.org/10.1016/0022-5096(95)00036-I)
- 1229 Perry, S. M., Lambert, V., & Lapusta, N. (2020). Nearly magnitude-invariant stress
 1230 drops in simulated crack-like earthquake sequences on rate-and-state faults
 1231 with thermal pressurization of pore fluids. *Journal of Geophysical Research: Solid Earth*, *125*(3), e2019JB018597. doi: 10.1029/2019JB018597
- 1232 Pharr, G. M., Herbert, E. G., & Gao, Y. (2010). The indentation size effect:
 1233 A critical examination of experimental observations and mechanistic in-
 1234 terpretations. *Annual Review of Materials Research*, *40*(1), 271-292. doi:
 1235 10.1146/annurev-matsci-070909-104456
- 1236 Rice, J. R. (1993). Spatio-temporal complexity of slip on a fault. *Journal of Geophysical Research: Solid Earth*, *98*(B6), 9885-9907. doi: 10.1029/93JB00191
- 1237 Rice, J. R. (2006). Heating and weakening of faults during earthquake slip. *Journal
 1238 of Geophysical Research*, *111*, B05311. doi: 10.1029/2005JB004006
- 1239 Rice, J. R., & Ruina, A. L. (1983). Stability of steady frictional slipping. *Journal of
 1240 Applied Mechanics*, *50*(2), 343-349.
- 1241 Rubin, A., & Ampuero, J.-P. (2005). Earthquake nucleation on (aging) rate and
 1242 state faults. *Journal of Geophysical Research: Solid Earth*, *110*(B11).
- 1243 Rubino, V., Rosakis, A. J., & Lapusta, N. (2017). Understanding dynamic friction
 1244 through spontaneously evolving laboratory earthquakes. *Nature Communications*, *8*(1), 15991. doi: 10.1038/ncomms15991
- 1245 Rubinstein, S. M., Cohen, G., & Fineberg, J. (2004). Detachment fronts
 1246 and the onset of dynamic friction. *Nature*, *430*(7003), 1005–1009. doi:
 1247 10.1038/nature02830
- 1248 Rubinstein, S. M., Cohen, G., & Fineberg, J. (2006). Contact area measurements re-
 1249 veal loading-history dependence of static friction. *Physics Review Letters*, *96*,
 1250 256103. doi: 10.1103/PhysRevLett.96.256103
- 1251 Ruina, A. (1983). Slip instability and state variable friction laws. *Journal of Geo-
 1252*

physical Research, 88(B12), 10359-10370.

- Schaal, N., & Lapusta, N. (2019). Microseismicity on patches of higher compression during larger-scale earthquake nucleation in a rate-and-state fault model. *Journal of Geophysical Research: Solid Earth*, 124(2), 1962-1990. doi: <https://doi.org/10.1029/2018JB016395>

Schmitt, S. V., Segall, P., & Dunham, E. M. (2015). Nucleation and dynamic rupture on weakly stressed faults sustained by thermal pressurization. *Journal of Geophysical Research: Solid Earth*, 120(11), 7606-7640. doi: [10.1002/2015JB012322](https://doi.org/10.1002/2015JB012322)

Schorlemmer, D., & Wiemer, S. (2005). Microseismicity data forecast rupture area. *Nature*, 434(7037), 1086–1086. doi: [10.1038/4341086a](https://doi.org/10.1038/4341086a)

Schwartz, D. P., & Coppersmith, K. J. (1984). Fault behavior and characteristic earthquakes—examples from the Wasatch and San Andreas fault zones. *Journal of Geophysical Research*, 89, 5681-5698.

Segall, P., & Rice, J. R. (1995). Dilatancy, compaction, and slip instability of a fluid-infiltrated fault. *Journal of Geophysical Research: Solid Earth*, 100(B11), 22155-22171. doi: [10.1029/95JB02403](https://doi.org/10.1029/95JB02403)

Segall, P., & Rice, J. R. (2006). Does shear heating of pore fluid contribute to earthquake nucleation? *Journal of Geophysical Research: Solid Earth*, 111(B9). doi: [10.1029/2005JB004129](https://doi.org/10.1029/2005JB004129)

Segall, P., Rubin, A. M., Bradley, A. M., & Rice, J. R. (2010). Dilatant strengthening as a mechanism for slow slip events. *Journal of Geophysical Research: Solid Earth*, 115(B12). doi: [10.1029/2010JB007449](https://doi.org/10.1029/2010JB007449)

Sibson, R. H. (1973). Interactions between temperature and pore-fluid pressure during earthquake faulting and a mechanism for partial or total stress relief. *Nature*, 243(126), 66-68.

Sibson, R. H. (1975). Generation of pseudotachylite by ancient seismic faulting. *Geophysical Journal of the Royal Astronomical Society*, 43(3), 775-794. doi: [10.1029/2018JB016395](https://doi.org/10.1029/2018JB016395)

- 1283 .1111/j.1365-246X.1975.tb06195.x
- 1284 Sieh, K. E. (1978). Central California foreshocks of the great 1857 earthquake. *Bulletin of the Seismological Society of America*, 68(6), 1731-1749.
- 1285
- 1286 Simons, M., Minson, S. E., Sladen, A., Ortega, F., Jiang, J., Owen, S. E., ... Webb, F. H. (2011). The 2011 magnitude 9.0 tohoku-oki earthquake: Mosaicking the megathrust from seconds to centuries. *Science*, 332(6036), 1421–1425. doi: 10.1126/science.1206731
- 1287
- 1288
- 1289
- 1290 Sone, H., & Shimamoto, T. (2009). Frictional resistance of faults during accelerating and decelerating earthquake slip. *Nature Geoscience*, 2(10), 705–708. doi: 10.1038/ngeo637
- 1291
- 1292
- 1293 Suppe, J. (2007). Absolute fault and crustal strength from wedge tapers. *Geology*, 35(12), 1127-1130. doi: 10.1130/G24053A.1
- 1294
- 1295 Svetlizky, I., & Fineberg, J. (2014). Classical shear cracks drive the onset of dry frictional motion. *Nature*, 509(7499), 205–208. doi: 10.1038/nature13202
- 1296
- 1297 Tanikawa, W., & Shimamoto, T. (2009). Frictional and transport properties of the chelungpu fault from shallow borehole data and their correlation with seismic behavior during the 1999 Chi-Chi earthquake. *Journal of Geophysical Research: Solid Earth*, 114(B1). doi: 10.1029/2008JB005750
- 1298
- 1299
- 1300
- 1301 Tenthorey, E., & Cox, S. F. (2006). Cohesive strengthening of fault zones during the interseismic period: An experimental study. *Journal of Geophysical Research: Solid Earth*, 111(B9). doi: <https://doi.org/10.1029/2005JB004122>
- 1302
- 1303
- 1304 Thom, C. A., Brodsky, E. E., Carpick, R. W., Pharr, G. M., Oliver, W. C., & Goldsby, D. L. (2017). Nanoscale roughness of natural fault surfaces controlled by scale-dependent yield strength. *Geophysical Research Letters*, 44(18), 9299-9307. doi: 10.1002/2017GL074663
- 1305
- 1306
- 1307
- 1308 Tinti, E., Scognamiglio, L., Michelini, A., & Cocco, M. (2016). Slip heterogeneity and directivity of the ML 6.0, 2016, Amatrice earthquake estimated with rapid finite-fault inversion. *Geophysical Research Letters*, 43(20).
- 1309
- 1310

- 1311 Tinti, E., Spudich, P., & Cocco, M. (2005). Earthquake fracture energy inferred
 1312 from kinematic rupture models on extended faults. *Journal of Geophysical Re-*
 1313 *search: Solid Earth*, 110(B12). doi: 10.1029/2005JB003644
- 1314 Tormann, T., Wiemer, S., & Mignan, A. (2014). Systematic survey of high-
 1315 resolution b value imaging along Californian faults: Inference on asperi-
 1316 ties. *Journal of Geophysical Research: Solid Earth*, 119(3), 2029-2054. doi:
 1317 <https://doi.org/10.1002/2013JB010867>
- 1318 Townend, J., & Zoback, M. D. (2000). How faulting keeps the crust strong. *Geology*,
 1319 28(5), 399-402. doi: 10.1130/0091-7613(2000)28(399:HFKTCS)2.0.CO;2
- 1320 Townend, J., & Zoback, M. D. (2004). Regional tectonic stress near the San Andreas
 1321 fault in Central and Southern California. *Geophysical Research Letters*, 31(15).
 1322 doi: 10.1029/2003GL018918
- 1323 Tsutsumi, A., & Shimamoto, T. (1997). High-velocity frictional properties of gabbro.
 1324 *Geophysical Research Letters*, 24(6), 699-702. doi: 10.1029/97GL00503
- 1325 Uchic, M. D., Dimiduk, D. M., Florando, J. N., & Nix, W. D. (2004). Sample
 1326 dimensions influence strength and crystal plasticity. *Science*, 305(5686), 986–
 1327 989. doi: 10.1126/science.1098993
- 1328 Wesnousky, S. G. (1994). The Gutenberg-Richter or characteristic earthquake dis-
 1329 tribution, which is it? *Bulletin of the Seismological Society of America*, 84(6),
 1330 1940-1959.
- 1331 Wibberley, C. A. J., Yielding, G., & Toro, G. D. (2008). Recent advances in the
 1332 understanding of fault zone internal structure: A review. In *The Internal
 1333 Structure of Fault Zones: Implications for Mechanical and Fluid-Flow Proper-
 1334 ties*. Geological Society of London. doi: 10.1144/SP299.2
- 1335 Wu, Y., & Chen, X. (2014). The scale-dependent slip pattern for a uniform fault
 1336 model obeying the rate- and state-dependent friction law. *Journal of Geophys-
 1337 ical Research: Solid Earth*, 119(6), 4890-4906. doi: 10.1002/2013JB010779
- 1338 Yamashita, F., Fukuyama, E., Mizoguchi, K., Takizawa, S., Xu, S., & Kawakata, H.

- 1339 (2015). Scale dependence of rock friction at high work rate. *Nature*, 528(7581),
1340 254–257. doi: 10.1038/nature16138
- 1341 Yasuhara, H., Marone, C., & Elsworth, D. (2005). Fault zone restrengthening
1342 and frictional healing: The role of pressure solution. *Journal of Geophysical*
1343 *Research: Solid Earth*, 110(B6). doi: <https://doi.org/10.1029/2004JB003327>
- 1344 Ye, L., Lay, T., Kanamori, H., & Rivera, L. (2016a). Rupture characteristics of
1345 major and great ($M_w > 7.0$) megathrust earthquakes from 1990 to 2015: 1.
1346 Source parameter scaling relationships. *Journal of Geophysical Research: Solid*
1347 *Earth*, 121(2), 826-844. doi: 10.1002/2015JB012426
- 1348 Ye, L., Lay, T., Kanamori, H., & Rivera, L. (2016b). Rupture characteristics of ma-
1349 jor and great ($M_w > 7.0$) megathrust earthquakes from 1990 to 2015: 2. Depth
1350 dependence. *Journal of Geophysical Research: Solid Earth*, 121(2), 845-863.
1351 doi: 10.1002/2015JB012427
- 1352 Zheng, G., & Rice, J. R. (1998). Conditions under which velocity-weakening friction
1353 allows a self-healing versus a crack-like mode of rupture. *Bulletin of the Seis-
1354 mological Society of America*, 88(6), 1466-1483.
- 1355 Zoback, M. D., Hickman, S., & Ellsworth, W. (2010). Scientific drilling into the San
1356 Andreas fault zone. *Eos, Transactions American Geophysical Union*, 91, 197-
1357 199. doi: 10.1029/2010EO220001